HHS Public Access

Author manuscript

Structure. Author manuscript; available in PMC 2023 January 06.

Published in final edited form as:

Structure. 2022 January 06; 30(1): 139–155.e5. doi:10.1016/j.str.2021.08.003.

Structure of the ancient TRPY1 channel from *Saccharomyces cerevisiae* reveals mechanisms of modulation by lipids and calcium

Tofayel Ahmed[1,a], **Collin R. Nisler**[2,3], **Edwin C. Fluck III**[1,4], **Sanket Walujkar**[3,5], **Marcos Sotomayor**[2,3,5], **Vera Y. Moiseenkova-Bell**[1,6,*]

[1]Department of Systems Pharmacology and Translational Therapeutics, Perelman School of Medicine, University of Pennsylvania, Philadelphia, Pennsylvania 19104, USA

[2]Biophysics Graduate Program, The Ohio State University, Columbus, Ohio 43210, USA

[3]Department of Chemistry and Biochemistry, The Ohio State University, Columbus, Ohio 43210, USA

[4]Biochemistry and Molecular Biophysics Graduate Group, Perelman School of Medicine, University of Pennsylvania, Philadelphia, Pennsylvania 19104, USA

[5]Chemical Physics Graduate Program, The Ohio State University, Columbus, Ohio 43210, USA

[6]Lead Contact

SUMMARY

Transient Receptor Potential (TRP) channels emerged in fungi as mechanosensitive osmoregulators. The *Saccharomyces cerevisiae* vacuolar TRP yeast 1 (TRPY1) is the most studied TRP channel from fungi, but the structure and details of channel modulation remain elusive. Here, we describe the full-length cryo-electron microscopy structure of TRPY1 at 3.1 Å resolution in a closed state. The structure, despite containing an evolutionarily conserved and archetypical transmembrane domain, reveals distinctive structural folds for the cytosolic N- and C-termini, compared to other eukaryotic TRP channels. We identify an inhibitory phosphatidylinositol 3-phosphate (PI(3)P) lipid-binding site, along with two Ca^{2+}-binding sites: a cytosolic site, implicated in channel activation and a vacuolar lumen site, implicated in inhibition. These findings, together with data from microsecond-long molecular dynamics simulations and a model

*Correspondence: V.M.-B. (vmb@pennmedicine.upenn.edu).

Author contribution

V.M-B. conceived the project. T.A. expressed and purified the protein. T.A. and E.C.F. prepared cryo-EM grids. E.C.F. collected cryo-EM data. T.A. processed cryo-EM data, built and refined the atomic model. C.R.N., S.W. and M.S. performed molecular dynamics simulation. T.A., E.C.F. and C.R.N. prepared figures. T.A., V.M-B., C.R.N. and M.S. wrote manuscript. All authors contributed toward the final edit.

[a]Present address: Department of Structural Biology, Max Planck Institute of Biophysics, Frankfurt am Main, Max von Laue Strasse 3, 60438, Germany

Declaration of interests

The authors declare no competing interests.

of a TRPY1 open state, provide insights into the basis of TRPY1 channel modulation by lipids and Ca^{2+}, and the molecular evolution of TRP channels.

Graphical Abstract

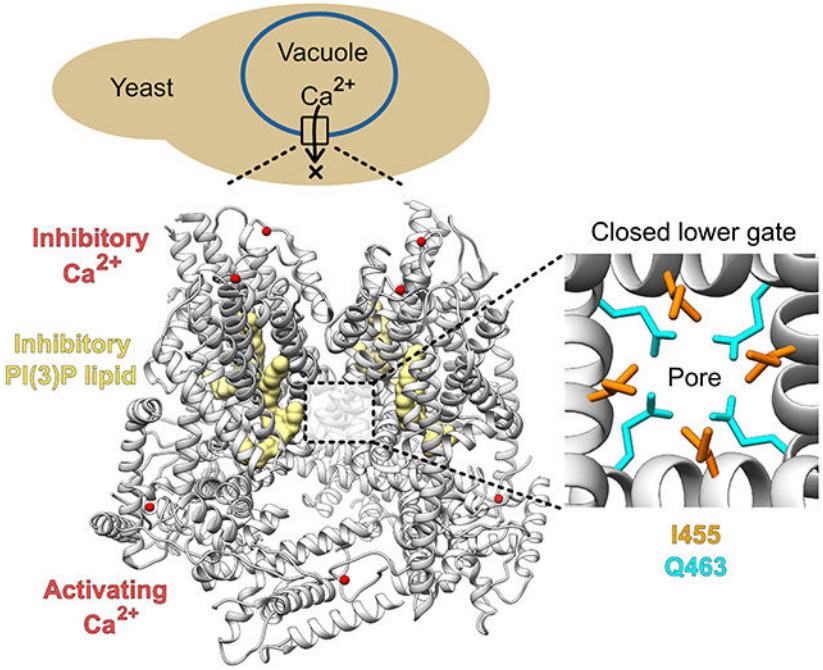

Blurb

Ahmed et al. describes a high-resolution structure of wild-type TRPY1 channel from *Saccharomyces cerevisiae* in a closed state. The authors captured the structure in the presence of one inhibitory PI(3)P lipid and two calcium ions, one involved in inhibition and the other in activation of the channel.

INTRODUCTION

Osmoregulation is the ability of cells to detect and counterbalance osmotic concentration variations in their surroundings(Hohmann, Krantz and Nordlander, 2007). In their natural environment, unicellular eukaryotic organisms like yeast, which live on plants and animals, can experience rapid water efflux (hyperosmotic shock) leading to shrinkage, or water influx (hypoosmotic shock) causing them to swell(Hohmann, Krantz and Nordlander, 2007). To survive hyperosmotic shocks, yeasts have been shown to release Ca^{2+} from intracellular stores to initiate a defense response that counterbalances rapid changes of osmotic concentration in their environment(Hohmann, 2002). One such source of Ca^{2+} is found in the vacuole, which acts as a Ca^{2+} buffering system that maintains low free cytosolic Ca^{2+} concentration in yeast(Cui et al., 2009). It has been reported that Ca^{2+} concentration in the yeast vacuole is around 1.3 mM, while cytosolic Ca^{2+} is only 260 nM(Halachmi and Eilam, 1989; Cui et al., 2009; Chang et al., 2010). Under osmotic challenges, ion

channels and transporters in the vacuole membrane are thought to work together to restore the osmotic balance.

The *Saccharomyces cerevisiae* vacuolar transient receptor potential yeast 1 (TRPY1, also known as yeast vacuolar conductance 1 or YVC1), considered the closest extant representative of the ancient state of eukaryotic TRP channels, has been shown to play a major role in Ca^{2+} release from the vacuole to the cytosol in response to hyperosmotic stress(Chang et al., 2010). TRPY1 is a non-selective Ca^{2+} permeable and polymodal cation channel, like many other TRP channels(Ramsey, Delling and Clapham, 2006; Julius, 2013; Hellmich and Gaudet, 2014; Rosasco MG, 2017). It was originally characterized as a Ca^{2+}-activated channel, but was later proposed to be also mechanosensitive(Bertl and Slayman, 1990; Bertl, Gradmann and Slayman, 1992; Zhou et al., 2003). Increased cytosolic Ca^{2+} concentration can enhance TRPY1 mechanosensitivity, consistent with its proposed *in vivo* function in osmotic regulation(Su et al., 2009; Hamamoto et al., 2018). Recently, it was shown that a high concentration of Ca^{2+} in the vacuolar lumen inhibits TRPY1 through Ca^{2+}-binding at the S5-S6 linker(Amini et al., 2019). TRPY1 can be also activated by reducing agents and inhibited by phosphatidylinositol 3-phosphate (PI(3)P), suggesting that reactive oxygen species and PI(3)P lipid are endogenous modulators of the channel(Hamamoto et al., 2018).

A recent comprehensive study on TRP channel mechanosensitivity has shown that the majority of mammalian TRP channels are insensitive to membrane stretch(Nikolaev et al., 2019). Nevertheless, a *Drosophila* TRP channel known as “No mechanoreceptor potential C” (NOMPC) has been shown unequivocally to be mechanosensitive both in *vitro* and in *vivo*(Zhang et al., 2015). Electrophysiological experiments suggest that TRPY1 is responsive to membrane stretch, indicating that both NOMPC and TRPY1 are mechanosensitive, although their activation mechanisms might be different(Su et al., 2009; Yan et al., 2013). A NOMPC structure revealed how its large ankyrin-repeat domain (ARD) organizes into a spring-like bundle that would interact with the cytoskeleton to control channel opening(Jin et al., 2017). In contrast, TRPY1 does not have an ARD, present in most mammalian TRP channels, or known connection to the cytoskeleton, which implies that channel activation might be triggered by membrane stretch sensed by its transmembrane core, or by Ca^{2+} binding to its cytosolic domain(Su et al., 2009, 2011).

To further understand the structural topology of this ancient eukaryotic TRP channel and to shed light on mechanisms of TRPY1 channel modulation, we determined the structure of the full-length TRPY1 channel in the presence of externally added Ca^{2+} by cryo-electron microscopy (cryo-EM). The transmembrane core of the channel revealed a “classic” TRP channel domain-swapped topology, but a hitherto not yet observed arrangement of N- and C-terminal domains contributed to a distinct overall architecture compared to other TRP channels. This structure further revealed a PI(3)P lipid binding site in the transmembrane region, along with two Ca^{2+}-binding sites per subunit, one at the cytosolic side and the other in the vacuolar lumen side. Insights from microsecond-long all-atom molecular dynamics (MD) simulations confirmed that PI(3)P and vacuolar Ca^{2+} play a central role in maintaining a closed state of the channel, while cytosolic Ca^{2+} is important for the structural integrity of the cytosolic N-terminal domain (NTD). A model for an open state suggests that a sustained

external stimulus such as membrane tension is required for channel activity, even in the absence of inhibitors. Overall, our findings provide structural insights that might guide the exploration of the molecular basis of TRPY1 channel modulation by hyperosmotic stress.

RESULTS

We overexpressed the full-length *Saccharomyces cerevisiae* TRPY1 channel in *Saccharomyces cerevisiae* and purified the channel using digitonin and glyco-diosgenin detergents. Since TRPY1 is activated by cytosolic Ca^{2+} between 10 μM to 1 mM and inhibited at 1 mM Ca^{2+} from the vacuolar luminal side(Amini et al., 2019), we determined TRPY1 structures in an apo condition at 3.0 Å and in a 2 mM Ca^{2+}-supplemented condition at 3.1 Å resolution by cryo-EM (Figures S1 and S2). Both of these cryo-EM density maps were of sufficient quality for *de novo* model building for the majority of the TRPY1 channel (Figures S1, S2, S3). These structures are nearly indistinguishable from each other (RMSD 0.307), including the bound Ca^{2+} ions and PI(3)P molecules (Figures S2). While Ca^{2+} was not added to the buffer solutions for the structure determined in the apo condition, there was still sufficient Ca^{2+} present that the channel was trapped in an apparently saturated Ca^{2+}-bound state. This may have been due to residual Ca^{2+} leeching from the filter paper during grid preparation, a possibility that has been reported in a separate cryo-EM study of inositol triphosphate receptors(Paknejad and Hite, 2018). As both TRPY1 structures appear to be in identical closed states, we will only discuss the 2 mM Ca^{2+}-supplemented state in this manuscript (Figures 1, S1, S2, S3, Table 1).

Similar to previously determined TRP channel structures(Cao et al., 2013; Gao et al., 2016; Hughes et al., 2018; Pumroy et al., 2020), TRPY1 forms a domain-swapped homo-tetramer with each subunit having a cytosolic N-terminal linker helical domain (LHD) consisting of eight tightly packed α-helices, six transmembrane α-helices (S1-S6) with a pore helix (P helix), followed by a TRP helix and a C-terminal domain (CTD) mainly comprising two long α-helices (Figure 1). Many TRP channels such as NOMPC, TRPA1, TRPM4, and TRPC6 have ARDs that form a large part of their cytosolic region (Figure 2a), but due to the absence of an ARD at the N-terminus of TRPY1, the entire cytosolic domain spanning LHDs and CTDs across the four TRPY1 subunits assumes the shape of a cytosolic “skirt” (Figure 1b), discussed in detail along with computational models in later sections. Although we worked with the full-length TRPY1 protein construct (Met1-Glu675), parts of the NTD (residues Met1-Asn24, Asp55-Glu65), the pre-S1 elbow (residues Leu216-Phe225), the loop between S3 and S4 helices (residues Pro323-Lys327), the TRP-CTD linker (residues Ala487-Ser529), and some parts of the C-terminal domain (residues Leu572-Ser580, Asp608-Glu675) were not resolved in our structure likely due to flexibility (Figure 1c, d) and models were not built for them (except for simulations as described below). We also did not build models for other ambiguous densities in the transmembrane region that are most probably annular lipids or detergent molecules. Overall, the TRPY1 structure has several “classical” TRP channel domains seen in other TRP channel structures (Figure 1c, d), yet there are specific features relevant for its regulation by Ca^{2+} and the channel’s role in mechanosensation in the yeast vacuolar membrane (Figure 1).

In our TRPY1 structure, the LHDs have distinct features in terms of the number and length of the helices, their relative arrangement, and the length of the LH5-LH6 loop (Figures 1c, 3a, b and 4a). Structural comparison to NOMPC (PDB: 5VKQ)(Jin et al., 2017), TRPM4 (PDB: 5WP6)(Winkler et al., 2017) and TRPC6 (PDB: 5YX9)(Tang et al., 2018) reveals conservation for the five LHD helices LH4-LH8 that are located adjacent to the pre-S1 helix (Figures 1c, d and 3b). However, LH3 in TRPY1 is two helical turns longer than in NOMPC, TRPM4 and TRPC6 (Figure 3b). Toward the N-terminus, like TRPM4, TRPY1 LHD has two more helices, LH1 and LH2. This is in contrast with NOMPC and TRPC6 where three such helices are present at the N-terminus, two of which are very short while the other is similar in length to LH2 of TRPY1. The LH5-LH6 loop (Arg154-Asn169) in TRPY1 is comparable to TRPC6 but longer than in NOMPC and TRPM4 (Figure 3b). Strikingly, the LH5-LH6 loop in TRPY1 interacts with the CTD of the neighboring subunit (discussed later) (Figures 3a and 4a). This loop-mediated interaction is a distinct feature of TRPY1's cytosolic skirt and is not observed in other TRP channels. Remarkably, this lengthy loop has a stable conformation and consequently a high-quality electron density, which allowed us to model all its side chains. The reason for this stability can be partly attributed to several interactions within the LHD such as three salt bridges between Arg155 and Glu172, Lys102 and Glu160, and Arg33 and Asp162 (Figure 4a). Coordination of a bridging cytosolic Ca^{2+} at the distal end of the LH5-LH6 loop provides additional stability (Figure 4a). In the absence of the ankyrin-repeat domains in TRPY1, the cytosolic skirt, especially the LHDs, may harbor the docking site for binding partners in the *S. cerevisiae* cytosol. Therefore, the structural differences in LHD helices along with the longer LH5-LH6 loop and its capability to coordinate a Ca^{2+} ion might have implications for TRPY1 channel function.

Another unique feature of the TRPY1 structure is the position of the CTD relative to the vacuolar membrane and the interaction of the CTD with the N-terminal LHD of a neighboring subunit (Figures 1b and 3a). The CTD is composed of a TRP-CTD linker that is not resolved in our cryo-EM structure, two long α-helices labeled CH1 and CH2, and a connecting CH1-CH2 loop (Figure 1). The CH1 helix is partially embedded in the membrane (Figure 1b) and connected to the CH2 helix by a loop that harbors the cytosolic Ca^{2+}-binding site (Figures 1b, c and 4a). This cytosolic Ca^{2+} is coordinated by backbone and side-chain oxygen atoms from Asp562, Thr563, Asp566 and Asp569 on the CH1-CH2 loop, as well as from Asn161 on the LH5-LH6 loop of the neighboring LHD (Figure 4a). Previously, it was suggested that the acidic patch of the four tandem aspartates between Asp573-Asp576 would comprise the cytosolic Ca^{2+}-binding site in TRPY1(Su et al., 2009) (Figures 3a and S4). Because we could not resolve the density for the seven amino acids between Asp574-Ser580 (Figures 3a and S4) due to flexibility, we cannot determine from our structure whether this acidic patch is indeed capable of binding Ca^{2+}. However, if a Ca^{2+} ion were to bind at this patch in our purified protein, then it would lead to a greater stabilization of the CH1-CH2 loop allowing us to elucidate the complete structure of the same loop. Moreover, mutagenesis and patch clamp studies reported that this acidic patch is not essential for Ca^{2+} activation of TRPY1(Hamamoto et al., 2018). Furthermore, the acidic patch is not conserved as revealed by a sequence alignment of TRPY channels from multiple fungal genomes (Figure S4). Therefore, it is unlikely that this acidic patch binds Ca^{2+} in

either recombinantly purified TRPY1 or in the vacuolar membrane of *S. cerevisiae*. Rather, TRPY1 activation by cytosolic Ca^{2+} is mediated by Ca^{2+}-binding at the subunit interface as discussed above, consistent with experimental results(Palmer et al., 2001; Hamamoto et al., 2018). Interestingly, Asn161 at the subunit interface is conserved among three (*S. cerevisiae* TRPY1, *K. lactis* TRPY2, *C. albicans* TRPY3) of the six sequences aligned across different fungal species (Figure S4). In the other three (*N. crassa, A. niger, A. flavus*), an acidic aspartate variation has replaced this asparagine and the CH1-CH2 loop (Arg553-Asp581) is shortened by 6-7 amino acids (Figure S4). The implications of this sequence variation and loop shortening in these three fungal genomes remain unknown, but our analyses suggest the presence of a similar cytosolic skirt structure and cytosolic Ca^{2+}-induced activation mechanism for at least TRPY1, TRPY2 and TRPY3.

The transmembrane domain of the channel was resolved to around 2.8 Å resolution (Figure S1f), which allowed us to visualize a lipid density that we assigned to PI(3)P (Figure 4b) and a small non-protein density that we assigned to a luminal Ca^{2+} (Figure 4c). The PI(3)P lipid was co-purified with the channel from yeast, as lipids were not added during purification. Endogenous yeast PI(3)P is typically found on the intraluminal vesicles of endosomes and vacuoles(Nascimbeni, Codogno and Morel, 2017), and it has been shown to inhibit TRPY1 channel activity(Hamamoto et al., 2018). The PI(3)P-binding site is located between the S1-S4 domain, the S4-S5 linker and the TRP helix of one subunit and S5 of an adjacent subunit (Figure 4b). The inositol ring of PI(3)P is positioned underneath the S1-S4 domain and is wedged above the TRP helix. In this position, the inositol ring interacts with TRP helix residues Arg483 and Gln479 via its 3' phosphate and 2' hydroxyl groups, respectively (Figure 4b). The PI(3)P position in this pocket is further stabilized by hydrogen bonding between Glu357 and the 5' hydroxyl on the inositol ring as well as between the backbone amine of Lys370 and the carboxyl from the ester moiety on one of the acyl tails of the lipid (Figure 4b). Apart from this, the 1' phosphate of PI(3)P maintains hydrogen bonding with the backbone amines of Phe298 and Trp299 and thus locks the hydrophilic headgroup of PI(3)P in position. The two acyl chains of PI(3)P branch out in a 'V' shape. One tail stabilizes in a cleft formed by S4 (containing a 3_{10}-helix) and the S4-S5 linker of one subunit and S5 and S6 of an adjacent subunit, through hydrophobic interactions. The other tail resides near the S4-S5 linker and we did not capture most of its density probably due to flexibility. A similar position for an inhibitory phosphatidylinositol lipid was observed in the TRPV1 structure(Gao et al., 2016), suggesting a conserved and ancient mechanism of lipid-mediated modulation among TRP channel homologues.

The luminal Ca^{2+}-binding site is formed by the loop connecting the S5 and P helices. The bound Ca^{2+} ion is coordinated by the side chains of residues Asp398, Asp401 and Asp405, as well as by the backbone carbonyls of Asp398 and Lys403 (Figure 4c). Since we have captured a closed state of TRPY1, this observation agrees with recent results(Hamamoto et al., 2018; Amini et al., 2019) that attribute an inhibitory role for luminal Ca^{2+} and describe Asp401 and Asp405 as responsible for Ca^{2+}-dependent inhibition of TRPY1. The functional importance of this Ca^{2+}-binding site is further underscored by the fact that the Gly402Ser mutation resulted in a constitutively active channel(Zhou et al., 2007). However, how the luminal Ca^{2+} leads to rearrangement of the S6 helix to stabilize the closed conformation of the channel remains to be elucidated. Perhaps the removal of the luminal Ca^{2+} would render

the P helix flexible, transmitting a gating signal to the pore in S6. We also observe some additional features in TRPY1 such as a π-hinge in the middle of S6, similar to some other TRP channels(Zubcevic and Lee, 2019; Huffer et al., 2020) and two proline residues, Pro432 and Pro433, at the beginning of S6 (Figures 2b, c, d, e and S4). In the absence of luminal Ca^{2+}, these features might have implications in channel gating by allowing more flexibility in S6.

It is interesting to note that the TRPY1 pore structure is almost identical to the NOMPC pore in a closed state, and similar to the pore structures of TRPA1, TRPM4 and TRPC6 (Figures 2b, c, d, e and 4d, e). Like all other TRP channels, the TRPY1 pore is comprised of a selectivity filter and a lower gate (Figure 4e). The selectivity filter is formed by the backbone carbonyl oxygen atoms of residues Leu419 and Gly420 (Figure 4d). Just above the selectivity filter, two negatively charged residues, Asp425 and Glu428, will attract and interact with luminal cations entering the pore. Overall, the luminal side of the pore is strongly negatively charged (Figure 3c, d, e) as luminal Ca^{2+}-binding site residues such as Asp398, Asp401 and Asp405 also line the surface (Figures 4c, d). The diameter of the selectivity filter is around 5.6 Å at the Gly420 carbonyl and is large enough to accommodate partially hydrated cations. This is similar to other TRP channels solved in the open state(Cao et al., 2013; Zhao et al., 2020). Therefore, although the selectivity filter is open in TRPY1, the pore is still closed to ion permeation due to a hydrophobic seal at Ile455 and due to Gln463, together forming the lower gate by constricting the pore diameter to 1.4 Å and 1.2 Å, respectively (Figure 4e).

Another interesting aspect of the TRPY1 structure is the network of interactions within each of the subunits that we identify as crucial in stabilizing the closed state of the channel (Figure 5). These interactions involve the TRP helix, the S4-S5 linker, the LHD, and the CH1-CH2 loop (Figure 5). The S4-S5 linker forms multiple contacts with the TRP helix which includes a salt bridge interaction between the side chains of Arg360 and Asp470, multiple hydrogen bonds between the side chain hydroxyl of Tyr473 and backbone amide of Arg360, and backbone carbonyls of Glu357 and Ser358 (Figure 5a). Evidently, Tyr473 is centrally positioned among these residues and the majority of its interacting partners are backbone atoms from the S4-S5 linker. Tyr473 is also conserved across the fungal genomes that we aligned (Figure S4). Together, these observations suggest that Tyr473 is a pivotal residue in the stabilization of the closed state of TRPY1. Earlier studies showed that mutations Tyr458His and Tyr473His increase the open probability of the channel(Zhou et al., 2007). These two mutants caused unstable open and closed states of the channel, suggesting their involvement in channel gating(Zhou et al., 2007). As deducible from our structure, the first mutation likely destabilizes the S6 helix with either a direct effect on the pore or an indirect effect on the stability of the Arg360-Asp470 salt bridge, or both. The second mutant directly disrupts the three hydrogen bonding interactions between the TRP helix and the backbone of the S4-S5 linker. Intriguingly, PI(3)P is positioned right next to the TRP helix and the S4-S5 linker and provides additional stability to this region, as discussed earlier (Figure 4b). Therefore, it is possible that the PI(3)P-interaction with the channel and channel gating are coupled in TRPY1. Finally, two salt bridges that are worth mentioning are formed within the same subunit between Arg190 and Arg197 from the LH8 of LHD with Asp557 and Glu560 from the CH1-CH2 loop of the CTD, respectively (Figure

5b). Together, these seem to stabilize the communication between the LHD and the CTD in each of the subunits. Overall, our structure indicates that there is an extensive network of salt bridges and hydrogen bonds between different domains of TRPY1 that play an important role in maintaining the closed state of the channel.

To further elucidate the roles of PI(3)P and Ca^{2+} in the stabilization of the TRPY1 closed conformation, we carried out all-atom MD simulations using the TRPY1 structure with missing parts incorporated as indicated in STAR Methods section. We built eight systems for simulation (Sim1 to Sim8 in Table S1), each representing a different potential state that the channel may exist *in vivo* or *in vitro*. Seven separate systems (Sim1 to Sim7 in Table S1) had the TRP-CTD linker (Ala487-Ser529) in a "vertical" configuration (Figure S5a-d). These include All-Bound (Sim1), in which all PI(3)P lipids and Ca^{2+} ions were present; None-Bound (Sim2), in which all were removed; No-Inh (Sim3), in which only the cytosolic Ca^{2+} sites were occupied while luminal Ca^{2+} ions and PI(3)P lipids were removed; the Y473H model (Sim4), in which this gain-of-function mutation(Su et al., 2007) (see "network of interactions within each of the subunits" above) was introduced to the No-Inh system in all four subunits; a fifth No-Ca^{2+} system with only PI(3)P bound and no Ca^{2+} (Sim5); a sixth double mutant (2-Mut; Sim6) system in which the Y473H and Y458H mutations were introduced to the No-Inh system; and a seventh 5-Mut system in which five gain-of-function mutations (Y473H, Y458H, F380L, S297W, and F247L) were introduced to the No-Inh system (Sim7). An eighth system featured the TRP-CTD linker in a "horizontal" configuration (Figure S5a-d) with all PI(3)P lipids and Ca^{2+} ions present. Each system was prepared and simulated with an identical protocol that included 100 ns of production simulations. Finally, two systems (Sim9 and Sim10) were constructed identically to Sim1 and Sim3, respectively, but were placed in a larger lipid patch for longer timescale simulations (see STAR Methods).

The All-Bound horizontal and vertical configurations exhibited noticeable differences in water permeation across the lipid bilayer during simulation (Figure S5e-j). When averaged over the entire simulation trajectory, some water density was observed within the lipid bilayer near the TRPY1 S1-S4 helices and the TRP-CTD linker in both systems, but to a far greater extent in the vertical configuration compared to the horizontal configuration (Figure S5e, g, h and j). This divergent behavior between the two models may help distinguish them in subsequent experimental studies. There is precedence for the facilitation of ion permeation across the lipid bilayer by similar domains from potassium channels, as the isolated voltage-sensing domain (VSD) of the Shaker Kv channel has been shown to form a cation selective pore(Zhao and Blunck, 2016). Voltage-dependent permeation of protons was also shown for the ion channel H_V1(Ramsey et al., 2006; Geragotelis et al., 2020), which has only four transmembrane helices in a VSD-like arrangement (S1-S4) with a predicted hydrated pathway(Geragotelis et al., 2020). The individual S1-S4 subunits of TRPY1 coupled to the TRP-CTD linker, and the CH1 helix featuring several charged residues at its N-terminus (Lys514 to Asp518), may function in a similar manner, explaining the observed water density. Although both vertical and horizontal configurations are feasible from a structural standpoint, we focused all subsequent analyses and discussion on our simulations of the channel with the TRP-CTD linker in the vertical configuration.

Simulations revealed that removal of PI(3)P resulted in early indications of pore opening and an overall increase in the dynamics of the TRPY1 structure. In the None-Bound, No-Inh, and all three mutation systems (Y473H, 2-Mut, 5-Mut), the S4 helix exhibits a greater degree of displacement from its initial position compared to the All-Bound system (Figure S6a-c). A similar result is seen for the S4-S5 linker (Figure S6d-f). The removal of PI(3)P thus facilitates displacement of key helices likely involved in gating and that may lead to opening of the pore at longer timescales (Figure S6a-f). The displacements in the S4 helix and the S4-S5 linker are more pronounced for the 2-Mut and 5-Mut systems, as these systems exhibited the greatest degree of deviation. This suggests that these mutations, when combined, can potentiate their influence on the dynamics of the transmembrane helices. Removal of PI(3)P also had an apparent effect on the dynamics of the TRP helix, as the distance between opposing TRP helices of diagonal subunits maintained a smaller separation in the All-Bound and No-Ca^{2+} systems compared to the remaining five systems, in which PI(3)P is not present (Figure S7a-c). These events may facilitate opening of the pore when PI(3)P is removed. Finally, removal of PI(3)P disrupted networks of allosteric communication between the different domains within the same subunit of TRPY1, as revealed by a dynamical network analysis(Sethi et al., 2009) (Figures S8 and S9). In the All-Bound system, the optimal path of allosteric communication from the N-terminus to the end of the S4-S5 linker (Gly26-Ser376) goes directly from the TRP helix to the S4-S5 linker through Tyr473 (Figure S8a, b), while in every other simulated system the optimal path does not pass through Tyr473 (Figure S8c-l), indicating that the presence of the PI(3)P lipid maintains a more compact network of communication between the TRP helix and the S4-S5 linker. Similarly, the optimal path from the end of the S4-S5 linker to Ile291 at the base of the S2 helix (chosen to observe the optimal path of allosteric communication between the pore and the periphery of the channel) first passes through the S3 and the S2 helix in the All-Bound system (Figure S9a-b). In the None-Bound, No-Inh, and Y473H systems, in which PI(3)P is not present, the optimal path does not pass through the S2-S3 helices (Figure S9c-h). All our analyses suggest that PI(3)P stabilized the closed state, perhaps by coupling S2 and S3. However, the introduction of either two or five gain-of-function mutations restored the communication between the S2 and S3 helices (Figure S9i-l), indicating that the gain-of-function mutations might trigger opening using a different mechanism than the wild type.

Analyses of interactions required for the stabilization of the closed state revealed that the Arg197-Glu560 salt-bridge was disrupted to a greater degree in simulations of the None-Bound and No-Inh systems relative to the All-Bound system (Figure S7d-f). Other interactions required for the stabilization of the closed state, such as Arg360-Tyr473 and Lys193-Tyr473, were disrupted by mobile lipid molecules from the bilayer (Figure S7g-i). As these lipid molecules formed interactions with one of the above-mentioned residues, the native intra-subunit interaction was disrupted, demonstrating the importance of the surrounding lipid environment to the function of TRPY1.

Next, we analyzed ion density by averaging the location of all K^+ ions over the 100-ns long trajectories for all systems. Significant differences between the All-Bound system and systems in which luminal Ca^{2+} is absent were recorded in the luminal entry to the pore above the selectivity filter (Figure 6a-n, s). This indicates that the removal of bound luminal

Ca^{2+} resulted in positively charged species spending more time interacting with the loops in this region. Over longer timescales, this effect could result in a greater probability of Ca^{2+} entry to the pore and a higher conductance. Mutated systems (Figure 6g-h, k-l, m-n) exhibit increased density below the selectivity filter formed by Leu419 and Gly420 compared to wild-type systems, suggesting that the increased dynamics of transmembrane helices in the mutants increases access of K^+ ions to the pore (Figure 6s).

As with the luminal Ca^{2+}-binding sites, Ca^{2+} binding to the cytosolic sites also affected the dynamics and permeation properties of the channel. The cytosolic ring loop between Val50-Ser68 forms the neck of the cytosolic skirt (Figures 1b and S7l) that may modulate cytosolic ion permeability. The dynamics of the cytosolic NTD depends on the presence of Ca^{2+} as revealed by simulations. In the None-Bound and No-Ca^{2+} systems, the distance between the center of mass of these loops in opposing subunits was smaller than for the systems in which the cytosolic Ca^{2+} is bound, and the N-terminal domain exhibited greater deviation from its starting position, indicating that Ca^{2+} "locks" these domains in place (Figures S7j-l and S6g-i, respectively). This is also revealed in the analysis of average pore radius over the entire trajectory (Figure 7). Closing of this cytosolic skirt constricts the pore radius within the skirt in the None-Bound and No-Ca^{2+} systems (Figure 7i), and provides a mechanistic explanation for how the presence of cytosolic Ca^{2+} leads to a higher open probability observed in experiments(Hamamoto et al., 2018; Amini et al., 2019).

The introduction of gain-of-function mutations had interesting effects on the dynamics of the TRPY1 structure. In the RMSD analyses of transmembrane and the TRP helices (Figures S6a-f and S7a-c), the 2-Mut and 5-Mut systems, and to a lesser extent the Y473H system, exhibited the greatest degree of divergence relative to the initial structure. These mutations destabilize the transmembrane region and could make the structure more susceptible to opening, either over longer timescales or in response to mechanical force. Additionally, the 2-Mut and 5-Mut systems had interesting effects on the cytosolic domain. Both had the highest RMSD divergence in the NTD (Pro32-Asp143) (Figure S6g-i), and the cytosolic ring loop distance was largest in these two systems (Figure S7j-l). While none of the mutations are located in the cytosolic domains, their effects propagate allosterically to the cytosolic portion of the protein. Finally, the 5-Mut system had the largest average pore radius at the Ser459, sandwiched between the lower gate formed by residues Ile455 and Gln463, indicating that these gain-of-function mutations are enough to see an initial opening of the pore even at 100 ns (Figure 7i).

To further validate the results of the 100-ns long simulations, the All-Bound and No-Inh systems embedded in larger membranes were equilibrated for 1200 ns (Sim9 and Sim10). In agreement with the results of the previous simulations, the RMSD analysis revealed a greater destabilization in the transmembrane helices for the No-Inh system compared to the All-Bound (Figure S10a-h). The pore radius of the No-Inh system also exhibited an increase both in the transmembrane portion, as well as in the cytosolic skirt (Figure 7j-l), indicating that removal of PI(3)P and luminal Ca^{2+} leads to a destabilization of the pore at longer timescales. The average radius within the lower-gate region of the channel (−10 Å to 15 Å) during the microsecond-long simulations indicates a wider pore in the No-Inh system (Figure 7l). Finally, the No-Inh system exhibited increased average K^+ density in the luminal

opening to the pore compared to the All-Bound system to a greater degree than in the 100 ns simulations (Figure 6o-s). These results suggest that the trends seen in the 100-ns long simulations can be extended to microsecond-long timescales, thus indicating that PI(3)P stabilizes a closed state, that luminal Ca^{2+} may electrostatically inhibit ion permeation, and that cytosolic Ca^{2+} is required to stabilize TRPY1's cytosolic skirt in a conformation favorable for ion conduction.

To obtain a model of the open state of TRPY1, an artificial and radially symmetric force was applied to the backbone atoms of the No-Inh system that were within a cylinder of 8-Å radius at the center of the pore (Figure 8a and Movie S1). We used this open state model and an external electric field(Gumbart et al., 2012) to simulate the channel under a transmembrane voltage of 0.5 V for 150 ns. While this voltage is large compared to physiological values of up to ~140 mV(Moldovan, Chapman-McQuiston and Wu, 2007), such values are routinely used to probe the conductance and gating of ion channels in short simulations(Aksimentiev and Schulten, 2005; Sotomayor et al., 2007; Jensen et al., 2012). The resulting K^+ permeation revealed a three-phased response, with an initial phase of 65 permeation events in 30 ns, an intermediate phase with 55 permeation events in 70 ns, and a final phase with only one permeation event for the remainder of the simulation (Figure 8b, d, g, j), corresponding to a conductance of 640 and 241 pS for the first and second phases, respectively. The second phase conductance agrees well with the experimentally measured conductance for TRPY1 of ~300 pS(Zhou et al., 2003),(Hamamoto et al., 2018)', (Palmer et al., 2001), suggesting that this conformation may reflect the structure and dynamics of TRPY1 in the open state recorded in experiments. The different phases result from successive closing of the pore (Figure 8b, d-f), which is driven by certain structural rearrangements in the helical domains. Rotation of the S4-S5 helices relative to one another (measured between the Cα carbons of residue 376) correlate with the drop of conductance observed for all phases, as does the closing and interaction of the basal portion of the S6 helix (measured between the center of mass of residues 458-462) (Figure 8g-l). Because these events result in the closure of the pore, their reversal may also be important for the gating of the channel in response to mechanical force. Intriguingly, these simulations also suggest that a sustained external stimulus, in addition to cytosolic Ca^{2+} and removal of PI(3)P, is required to keep the channel open.

Despite the rapid closure of TRPY1 in our simulations, we observed multiple permeation events of K^+ ions that were facilitated by several pore-spanning residues. The backbone oxygen atoms of Leu419 and Gly240, as well as the side chain of Tyr443, initially sequestered K^+ ions to the mouth of the pore and shuttled them to a vestibule formed by the backbone oxygen atoms of Ser447 and Leu451, as well as the side chain of Asn452. From here, the ions passed through the lower gate formed by the backbone oxygen atoms of Ile455 and the side chain of Gln463. The side chain of Ser459 also facilitated this passage through the lower gate. All these residues worked in concert to maintain a continuous network of interactions with K^+ ions throughout the length of the pore (Figure 8c and Movie S2).

DISCUSSION

TRP channels are best represented by the 28 family members in mammals that are activated by a variety of physical stimuli and compounds, and behave in a polymodal manner. Since 2003, structures for representative members from almost all mammalian TRP channel families have been determined(Huffer et al., 2020; Pumroy et al., 2020), yet a common theme underlying channel gating is far from established. Therefore, TRPY1 from single-celled yeast can serve as the archetypical TRP channel to help elucidate the intricacies of TRP channel gating and modulation. One could imagine that such knowledge only increases in complexity as we study the TRP channels from multicellular organisms. The high-resolution structure of the ancestral TRPY1 channel presented here, therefore, serves as a stepping-stone towards understanding TRP channels' evolution and TRPY1 gating modulated by Ca^{2+}, lipids, and membrane stretch in fungi.

Several unique structural features of TRPY1 are likely to be relevant for channel gating. The TRP-CTD linker and the CH1 helices are tucked against the S1-S4 bundles, and in our model insert into the membrane significantly (Figure 1b, c). This arrangement provides a direct connection between the TRP helix, the periphery of the channel and the surrounding lipid bilayer, which could be relevant for mechanisms of mechanosensation involving force from lipids(Teng et al., 2015). In addition, the CH1 helix wraps on the back of the pre-S1 helix to connect to the cytosolic Ca^{2+}-binding site and CH2, which in turn interacts with the periphery of the neighboring subunit's LHD, a unique arrangement not seen in any other TRP channel. The stabilization of this architecture by the cytosolic Ca^{2+} that activates the channel further implicates the TRP helix in channel gating.

The two Ca^{2+}-binding sites revealed in our TRPY1 structure are distinct from those found in other TRP channels that are confined to a cavity between the S2 and S3 helices, and the S2-S3 linker that resides in the membrane region(Autzen et al., 2018; Diver, Cheng and Julius, 2019; Zhao et al., 2020). Rather, in each TRPY1 subunit, one Ca^{2+} binds to the cytosolic side and another Ca^{2+} binds at the vacuolar lumen side (Figure 4a, c). It is fascinating that the two Ca^{2+}-binding sites orchestrate opposite effects on the channel gating, the vacuolar lumen site being inhibiting and the cytosolic site being activating(Hamamoto et al., 2018; Amini et al., 2019). Simulations presented here offer insights into the possible mechanistic explanations for the experimental results(Amini et al., 2019) concerning the role of the Ca^{2+} ions. Removal of cytosolic Ca^{2+} resulted in a domain constriction and a more occluded pore radius in this region (Figures 7 and S7j-l). Removal of luminal Ca^{2+}, however, led to an increase in the presence of K^{+} at the cusp of the pore (Figure 6a, c, s), demonstrating how these unique Ca^{2+}-binding sites can modulate channel activity on a molecular scale.

All sites were fully occupied by Ca^{2+} in our TRPY1 structure captured in a closed state, but it appears that only the vacuolar lumen site would remain occupied in the native yeast conditions that favor channel closure. Channel activation may require removal of Ca^{2+} from the vacuolar lumen site to create a Ca^{2+}-flux directed from the vacuole to the cytosol. Yet, the concentration of Ca^{2+} in the vacuole is 3,000 times higher than in the cytosol under normal conditions(Halachmi and Eilam, 1989; Cui et al., 2009; Chang et al., 2010). It has been argued that vacuolar free-Ca^{2+} is scarce, as most Ca^{2+} ions are bound to vacuolar

polyphosphate(Dunn, Gable and Beeler, 1994), thus adding another layer of complexity to TRPY1 function in calcium-induced calcium release (CICR) feedback loops *in vivo*.

The TRPY1 structure reported here is in a closed state. Given that PI(3)P lipids are strongly bound to the channel, we suggest that an abundance of PI(3)P in the vacuole keeps TRPY1 in its closed conformation. The presence of PI(3)P in the observed binding site brings the TRP helix closer to the S4-S5 linker through interactions between Tyr473 and Arg360 residues. The destabilization of this interaction, which is probably the cause of gain-of-function(Su et al., 2007) in the TRPY1 Y473H mutant, might lead to opening of the channel upon application of different endogenous stimuli that are proposed to gate TRPY1. Our proposed model is in agreement with the notion that the S4-S5 linker is the "gear box" conveying gating force in TRP channels and suggests that TRP channels maintained a conserved gating mechanism throughout evolution. This is supported by simulations, in which the removal of PI(3)P had several effects on the dynamics and interactions implicated in channel activity. In particular, allosteric communication between the NTD and the S4-S5 linker was directly mediated by the Tyr473-Arg360 interaction only when PI(3)P was present (Figure S8), and removal of PI(3)P disrupted communication between the S2 and S3 helices in the transmembrane domain in the wild type protein (Figure S9). It is conceivable that mechanical force generated by hyperosmotic shocks in yeast could induce the release of PI(3)P lipids from their binding sites, thus facilitating opening of the channel and Ca^{2+} flow from the vacuole to the cytosol to start a hyperosmotic shock defense mechanism in yeast (Figure 9).

The open state of TRPY1 has a conductance >300 pS (180 mM KCl), suggesting that gating requires conformational changes that can lead to a pore opening of as much as 10 Å in diameter estimated using Hille's equation(Cruickshank et al., 1997; Hille, 2001). Simulations presented here, in which voltage is applied to a hypothetical open state model, offer potential insights into these conformational changes, and result in a conductance similar to that observed in experiments when the minimum radius is ~2 Å. From these simulations it is apparent that the dynamics of the S4-S5 linker and the basal portion of the S6 helix are important for gating the channel. It is tempting to speculate that mechanical force from lipids is communicated through the TRP-CTD linker and the S1-S4 domains to the TRP and S4-S5 linker helices to gate the channel, and that this requires an intact cytosolic skirt with bound Ca^{2+}. However, how various parts of TRPY1 re-arrange to accommodate a larger pore that can sustain its large conductance remains to be decisively elucidated.

STAR METHODS

RESOURCE AVAILABILITY

Lead Contact—Further information and requests for either resources or reagents should be directed to and will be fulfilled by the lead contact Vera Moiseenkova-Bell (vmb@pennmedicine.upenn.edu).

Materials Availability—Requests for materials generated in this study should be directed to and will be fulfilled by the lead contact Vera Moiseenkova-Bell (vmb@pennmedicine.upenn.edu).

Data and Code Availability—All data generated in these studies are available upon request from lead contact Vera Moiseenkova-Bell (vmb@pennmedicine.upenn.edu). The cryo-EM density map and the atomic coordinate of PI(3)P and Ca^{2+}-bound full-length TRPY1 in detergent are deposited into the Electron Microscopy Data Bank and Protein Data Bank under accession codes EMD-21672 and 6WHG. To avoid repetition, we have not submitted the apo condition map and model in the databases. This paper does not report original code. Any additional information required to reanalyze the data reported in this paper is available from the lead contact upon request.

EXPERIMENTAL MODEL AND SUBJECT DETAILS

For expression of TRPY1 channel, BJ5457 *Saccharomyces cerevisiae* (ATCC) was transfected with a YepM plasmid bearing TRPY1 sequence. Additional details can be found in the Method Details.

METHOD DETAILS

Protein expression and purification—Wild type TRPY1 containing YepM plasmid(Moiseenkova-Bell et al., 2008) was transfected into BJ5457 *Saccharomyces cerevisiae* (ATCC) for constitutive expression of the protein. The cells were grown at 30°C until OD_{600} reached mid log phase (1.2-1.4) and thereafter harvested to store at −80°C for future use. Steps hereafter were carried out at 4°C. Membranes containing expressed TRPY1 were prepared by thawing the cells on ice and breaking them using a M110Y microfluidizer (Microfluidics) in homogenization buffer containing 25 mM Tris-HCl, pH 8.0, 300 mM Sucrose and 5 mM EDTA and protease inhibitor cocktail (Sigma). Membranes were then pelleted by first discarding cellular debris with 3,000 x *g* and 14,000 x *g* centrifuge runs, then 100,000 x *g* ultra-centrifugation to pellet the membranes before storing them in 5 mM Tris-HCl, pH 8.0, 300 mM Sucrose and 1 mM PMSF. The membranes were solubilized in 20 mM HEPES pH 8.0, 150 mM NaCl, 10% glycerol, 1% digitonin, 2 mM TCEP, and 1 mM PMSF for 2 h. Insoluble material was removed via ultra-centrifugation at 100,000 *x g* and the solubilized TRPY1 was purified by binding to 1D4 antibody coupled to CnBr-activated Sepharose beads. The beads were used to make a column and extensively washed with Wash Buffer containing 20 mM HEPES pH 7.5, 150 mM NaCl, 0.01% glyco-diosgenin and 2 mM TCEP. The protein was eluted from the column with Wash Buffer supplemented with 3 mg mL^{-1} 1D4 peptide and concentrated to 4.3 mg mL^{-1} using a 100-kDa concentrator (Millipore) before further purifying by size exclusion chromatography using a Superose 6 increase 10/300 GL column (GE Healthcare). The eluted protein was concentrated to 2 mg mL^{-1} and used for vitrification.

Specimen preparation and cryo-EM data acquisition—Prior to preparing cryo-EM grids, purified protein was incubated with 2 mM $CaCl_2$ for 10 min. This sample was blotted once (3.5 mL per blot) onto glow discharged 200 mesh Quantifoil 1.2/1.3 grids (Quantifoil Micro Tools) at 4°C and 100% humidity and plunge frozen in liquid ethane cooled to the

temperature of liquid nitrogen (Thermo Fisher Vitrobot Mark IV). Cryo-EM images were collected using a 300 kV Thermo Fisher Krios microscope equipped with a Gatan K3 direct detector camera in super resolution mode. Forty frame movies were collected with a total dose of 45 e/ $Å^2$ and a super resolution pixel size of 0.53 Å/pix. Defocus values of the images ranged from −0.5 to −2.5 μm.

Image processing—Relion 3.1 (version: beta-commit-b86482)(Scheres, 2012, 2016; Zivanov et al., 2018) was used for data processing of 11,099 super-resolution image stacks (Figure S3a). Relion's implementation of MotionCor2(Zheng et al., 2017b; Zivanov et al., 2018) was employed to compensate for beam-induced movement and to set the pixel size to 1.06 Å following 2×2 binning. CTFFIND-4.1(Rohou and Grigorieff, 2015) was used to estimate CTF parameters. Laplacian-of-Gaussian autopicking was performed on a small subset (100) of the motion-corrected images followed by two rounds of 2D classification to obtain representative templates for autopicking from the full dataset. Thus, 20,947 initial particles were autopicked, which after two rounds of 2D sorting yielded the best representative template for autopicking on the complete dataset. Autopicking on complete dataset yielded ~3.1 million particles. These particles were 4x-binned and subjected to two rounds of 2D sorting to discard false positives and bad particles. The remaining class averages containing 254,509 particles showed clear signs of being originated from a tetrameric TRP-like channel. These particles were 2x-binned and used to generate an initial model that was subsequently used as a reference to perform a 3D classification with six classes. One class among these six, containing 100,918 particles, aligned well and therefore was better resolved than the rest. Using the map from this class, a loose mask was generated surrounding the tetramer and detergent belt, and thereafter used for 3D refinement and 3D classification of 100,918 unbinned particles applying C4 symmetry and mask. One among the three 3D classes generated, containing 55,593 particles, was subsequently 3D refined to obtain a 3.93 Å map which was then subjected to CTF refinement with corrections for higher-order aberration, anisotropic magnification and per particle defocus, and Bayesian polishing. 3D refinement after Bayesian polishing yielded a 3.35 Å map. A second round of CTF refinement and Bayesian polishing, and a subsequent 3D refinement generated a 3.19 Å map which after postprocessing yielded a 3.08 Å map. This 3.08 Å map was used to build atomic models. The local resolution map was generated using Relion(Zivanov et al., 2018).

Model building and refinement—An initial model for a single subunit of the full length TRPY1 was generated using the online server ITASSER(Roy, Kucukural and Zhang, 2010; Yang and Zhang, 2015). This model was roughly partitioned into cytosolic, transmembrane and C-terminal domains and rigid body docked into their respective densities. Except for the transmembrane domain, which showed satisfactory fitting, the other two domains did not fit well and therefore were manually adjusted in COOT(Emsley and Cowtan, 2004) to fit the density. The quality of density was comparatively lower in the C-terminal domain and therefore extra care was taken to account for correct registers in the side chain assignments. To assign side chains in the C-terminal helix CH1 and the loop thereafter, spanning Lys517-Asp573, confidence was derived from the distinctive identity of the bulky side chains from Lys538, Arg541, Arg544, Arg545, Tyr548, Arg550, Tyr561, Trp565, Tyr571 and the kinks produced by Pro530 and Pro564. Due to poorer density for CH2 helices, the side chain

placements were done based on the original I-TASSER model. A model for the PI(3)P lipid was built in COOT and thereafter the eLBOW(Moriarty, Grosse-Kunstleve and Adams, 2009b) tool from the PHENIX(Adams et al., 2002) software package was used to generate restraints for refinement. Models for Ca^{2+} ions were generated in COOT and were kept unlinked to the protein during refinement. The complete model was then iteratively refined using phenix.real_space_refine from the PHENIX(Adams et al., 2002) software package with secondary structure and NCS restraints for the protein and eLBOW-generated restraints for PI(3)P. In the final model, side chains for Leu216, Phe225, Leu572, Asp573 and Lys517-Ser529 were pruned due to insufficient density. Model validation was carried out in Molprobity(Chen et al., 2010b) and EMRinger(Barad et al., 2015). For cross-validation, each final model was randomized by 0.5 Å in PHENIX(Adams et al., 2002) and refined against a single half map. These models were converted into volumes in Chimera(Pettersen, 2004) and then EMAN2.1(Bell et al., 2016) was used to generate FSC curves between these models and each half map as well as between each final model and the final maps. HOLE(Smart et al., 1996) was used to generate the pore radii. Electrostatic potential was calculated using APBS-PDB2PQR(Dolinsky et al., 2004). Figures were prepared using PyMOL(Schrodinger, 2015) and Chimera(Pettersen, 2004) software.

TRPY1 molecular dynamics simulations and analyses—The cryo-EM structure of TRPY1 generated in the current study (PDB: 6WHG) was modified as described below and thereafter used for all MD simulations and their associated analyses. The cryo-EM structure has seven missing segments in each chain due to a lack of electron density, from residues Met1-Asn24 (segment 1; N-terminus), Asp55-Glu65 (segment 2; loop in cytosolic skirt), Leu216-Phe225 (segment 3; pre-S1 elbow), Pro323-Lys327 (segment 4; loop between S3 and S4 helices), Ala487-Ser529 (segment 5; TRP-CTD linker), Leu572-Ser580 (segment 6; part of C-terminus), and Asp608-Glu675 (segment 7; C-terminal tail). Segments 1 and 7 were not included in our models. Segments 3, 4, and 6 were built using the interface to the Modeller server in Chimera(Pettersen, 2004), which returned all as unstructured loops. The top result for each was taken directly from the Modeller output and was then minimized in vacuum for 10,000 steps in NAMD(Phillips et al., 2005, 2020) with constraints placed on all but the modeled segments (this and subsequent harmonic constraints used $k = 1$ kcal mol^{-1} $Å^{-2}$). Real space refinement was performed on the resulting model to better fit the cryo-EM map. Segment 2 was built as a loop in COOT(Emsley and Cowtan, 2004), based on the cryo-EM map with C4 symmetry applied and no sharpening. This was then minimized in vacuum for 50,000 steps in NAMD with all but segment 2 constrained. Minimization of all modeled segments allowed side chains to explore different conformations and reach an orientation that locally minimizes energy. Because segment 5 was predicted to contain a helix based on its sequence, this segment was submitted to the Phyre2 homology-modeling server(Kelley et al., 2015). The top model from Phyre2 contained an amphipathic helix and this model was inserted, un-altered, into the TRPY1 structure using COOT. The helix was placed based on constraints imposed by flanking residues that were present in the initial cryo-EM structure, as well as on the matching of the hydrophilic surface of the helix with a hydrophilic patch on the face of the protein. This segment was then minimized in vacuum for 10,000 steps in NAMD with all but segment 5 constrained. This was done for a single chain. To insert the missing segments into the remaining three chains, the completed chain

was aligned to the other three chains in COOT, and the coordinates of the missing segments were saved. These were then inserted into the remaining chains, and all completed chains were saved as a single model, which was then vacuum minimized for 50,000 steps in NAMD, with all but the missing segments constrained.

The TRPY1 structure (PDB: 6WHG) also contains four PI(3)P molecules bound as ligands with a partial missing tail in each. To complete these ligands, the internal coordinates from the SAPI13 molecule in the toppar_all36_lipid_inositol.str CHARMM parameter file were used with the autopsf plugin. The entire structure was then vacuum minimized in NAMD for 50,000 steps with all but the PI(3)P molecules constrained. The final coordinates were saved, and this entire structure was embedded in a 150 × 150 Å membrane patch that contained 50% POPC, 18% POPA, 16% POPS, and 16% POPI. The membrane patch was generated using the Membrane Builder function on the CHARMM-GUI server. Both leaflets were built using the same composition of lipids, and this composition was chosen based on experimental observations(Tsuji and Fujimoto, 2018). The transmembrane region was placed based on hydrophobic regions of the core helices, proximity of tryptophan residues to lipid head groups, and previous simulations performed on TRP channels(Sakipov, Sobolevsky and Kurnikova, 2018; Wang et al., 2020). Then, the solvate plugin in VMD(Humphrey, Dalke and Schulten, 1996) was used to add TIP3P water molecules to the system, and the autoionize plugin was used to neutralize the system and add KCl to a final concentration of 150 mM.

Simulations were run using NAMD 2.12(Phillips et al., 2005, 2020) and the CHARMM36 force field(Vanommeslaeghe and Mackerell, 2015). The TIP3P(Jorgensen et al., 1983) explicit model of water was used. Long-range electrostatic forces were computed using the Particle Mesh Ewald method with a grid point density of >1 $Å^{-3}$, and a cutoff of 12 Å was used for van der Waals interactions with force switching and a switching distance of 10 Å. The SHAKE algorithm was used with a timestep of 2 fs. The *NpT* ensemble was used at 1 atm with a hybrid Nosé-Hoover Langevin piston method and a 200 fs decay period, with a 50 fs damping time constant. The completed simulation system was minimized for 1,000 steps, followed by a lipid-melting step in which all but the lipid tails were constrained for 0.5 ns of equilibration. This was followed by 0.5 ns of equilibration in which the protein was constrained and the water, lipids, and ions were free. Next, constraints were released on the modeled segments of the protein for 10 ns, allowing them to equilibrate with their surroundings. Finally, all constraints were lifted and the system was run for 26.4 ns using a Langevin damping coefficient of $\gamma = 1$, after which γ was set to 0.1 for 100 ns of free equilibration. All analyses were performed on the final 100 ns for every simulation run at 300 K. Coordinates were saved every 2 ps.

A total of 10 simulation systems were prepared and run as described above. The first seven are variations of a “vertical” configuration, in which the TRP-CTD linker was modeled with its helical segment lying vertically across the membrane (Figure S5a-d). The first is the All-Bound system, in which all Ca^{2+} and PI(3)P sites are occupied (Table S1, Sim1). The second is the None-Bound system, in which all Ca^{2+} and PI(3)P are removed (Sim2). For the third system, labeled No-Inh, only the non-inhibitory (cytosolic) Ca^{2+}-binding sites remain occupied, while the PI(3)P and the inhibitory (luminal) Ca^{2+} ions were removed

(Sim3). In the fourth system, a gain-of-function Y473H mutation was introduced to the non-inhibitory system using VMD's Mutate Residue plugin (Sim4). The fifth system is devoid of any Ca^{2+} but contains the bound PI(3)P molecules (Sim5). The sixth and seventh systems, respectively, are a double mutant (2-Mut), in which mutations Y473H and Y458H are introduced, and a five-mutant system (5-Mut), in which mutations Y473H, Y458H, F380L, S297W, and F247L are introduced to the No-Inh system (Sim6 and Sim7 systems, respectively).

An additional system (Sim8) was built based on the "horizontal" configuration of the TRP-CTD linker, in which the amphipathic helix of segment 5 (TRP-CTD linker) was modeled as laying horizontally at the membrane-cytosolic interface (Figure S5a-d). This system, besides segment 5, is identical to the All-Bound system of the vertical configuration (Sim1).

Two final systems were generated exactly as described above for the All-Bound and No-Inh models, but inserted in a larger lipid patch and prepared for Anton2 simulations(Shaw et al., 2008). While the lipid composition remained the same, the bigger patch for these two systems measures 165 × 165 Å (Sim9 and Sim10). These systems were minimized and equilibrated identically to the previous systems but with 11 ns of free equilibration, for a total of 22 ns, and were used as the starting point for production MD on the Anton supercomputer. Snapshots of these systems at 22 ns were converted to Anton2 compatible dms file format using the convertNAMDtoDMS.py script provided by PSC. Anton2 simulations used the same force field as NAMD simulations (CHARMM36). Simulations were performed in the *NpT* ensemble (300 K, 1 atm) using the Nosé-Hoover thermostat, the Martyna-Tobias-Klein barostat and semi-isotropic pressure coupling. The multigrator integration framework(Lippert et al., 2013) was used with a 2.5 fs timestep along with a barostat period of 480 steps and a thermostat period of 24 steps. The SHAKE algorithm was used to fix hydrogen atoms and van der Waals interactions were calculated with a cutoff of 12 Å, while long range electrostatic interactions were calculated using u-series electrostatics with a 64 × 64 × 128 grid. Coordinates of the trajectories were saved every 120 ps.

The network analysis was performed following standard protocols(Sethi et al., 2009) using the 100-ns long trajectories. First, a dynamic network is created from the MD trajectory in VMD using Carma(Glykos, 2006), a program that calculates correlation of motion between atoms in an MD simulation. Optimal and suboptimal paths are calculated by first choosing a source and a sink node, and the communication pathways between these nodes are calculated for the minimal number of nodes. Those nodes that occur in the most sub-optimal paths are critical nodes for allosteric communication between source and sink nodes. All visualization of molecular images and allosteric pathways was performed in VMD. Ion and water densities were calculated using the VolMap tool plugin in VMD with a resolution of 1 Å. The average density was computed and combined for all frames with no weight after alignment. These data, given in number of atoms/$Å^3$, were then converted to a contour map and reported in molarity. To quantify ion density the volumetric data was averaged over a series of *x,y* planes along the *z* axis in MATLAB and plotted (Figure 6s).

For each frame of the given simulation, RMSD was calculated based on the alignment of a selection of Cα atoms to the same selection of atoms in the first frame of the trajectory. In this way, the RMSD analysis of every system was done based on the same starting structure.

The average pore radius (Figure 7) was calculated using the program HOLE(Smart et al., 1996). After alignment of the protein to the first frame of the trajectory, HOLE calculates the pore radius in every frame of the trajectory along the path of the pore in the *z*-dimension. Next, these values are averaged throughout the trajectory at each position in the pore, with error bars in Figure 7 indicating the standard deviation.

To create an open state model (Sim11) we applied for ~20 ns a radially symmetric force of 5 kcal/(mol·Å) (210 pN) to protein backbone atoms that were within a cylinder of 8-Å radius at the pore center. This was done using the equilibrated conformation obtained at the end of the 100 ns equilibration of the No-Inh system (Sim3). Membrane voltage was simulated by applying an external electric field of 11.52 kcal/(mol·*e*) perpendicular to the membrane and normalized by the size of the box along the *z*-axis, corresponding to a membrane voltage of 0.5 V (Sim12).

QUANTIFICATION AND STATISTICAL ANALYSIS

Cryo-EM data were processed using RELION(Scheres, 2012). Cryo-EM structural statistics were analyzed by Phenix(Adams et al., 2002), Molprobity(Chen et al., 2010a), EMRinger(Barad et al., 2015) and UCSF Chimera(Pettersen, 2004). Standard deviation is used to create error bars in Figure 7. Statistical details are explained in METHOD DETAILS or figure legends.

Supplementary Material

Refer to Web version on PubMed Central for supplementary material.

Acknowledgements

We thank Sabine Baxter for assistance with hybridoma and cell culture at the University of Pennsylvania Perelman School of Medicine Cell Center Services Facility. We acknowledge the use of instruments at the Electron Microscopy Resource Lab and at the Beckman Center for Cryo Electron Microscopy at the University of Pennsylvania Perelman School of Medicine. We also thank Darrah Johnson-McDaniel for assistance with Krios microscope operation. This work was supported by grants from the National Institute of Health (R01GM103899 and R01GM129357 to VYM-B). Use of TACC-Stampede2 and PSC-Bridges supercomputers was supported by the National Science Foundation through XSEDE (XRAC MCB140226 to MS). Use of Anton2 was supported by grant MCB190084P to MS. Use of resources at the Ohio Supercomputer Center was supported by grants PAS1037 and PAA0217 to MS. CN was supported by an OSU/NIH molecular biophysics training grant (T32GM118291).

REFERENCES

Adams PD et al. (2002) ‘PHENIX: Building new software for automated crystallographic structure determination’, Acta Crystallographica Section D: Biological Crystallography, 58(11), pp. 1948–1954. doi: 10.1107/S0907444902016657. [PubMed: 12393927]

Aksimentiev A and Schulten K (2005) ‘Imaging alpha-hemolysin with molecular dynamics: ionic conductance, osmotic permeability, and the electrostatic potential map.’, Biophysical journal, 88(6), pp. 3745–3761. doi: 10.1529/biophysj.104.058727. [PubMed: 15764651]

Amini M et al. (2019) ‘Identification of Inhibitory Ca2+ Binding Sites in the Upper Vestibule of the Yeast Vacuolar TRP Channel’, iScience. 2018/12/04, 11, pp. 1–12. doi: 10.1016/j.isci.2018.11.037. [PubMed: 30572205]

Autzen HE et al. (2018) ‘Structure of the human TRPM4 ion channel in a lipid nanodisc’, Science, 359(6372), pp. 228–232. doi: 10.1126/science.aar4510. [PubMed: 29217581]

Barad BA et al. (2015) ‘EMRinger: Side chain-directed model and map validation for 3D cryo-electron microscopy’, Nature Methods, 12(10), pp. 943–946. doi: 10.1038/nmeth.3541. [PubMed: 26280328]

Bell JM et al. (2016) ‘High resolution single particle refinement in EMAN2.1’, Methods. 2016/2/27, 100, pp. 25–34. doi: 10.1016/j.ymeth.2016.02.018. [PubMed: 26931650]

Bertl A, Gradmann D and Slayman CL (1992) ‘Calcium- and voltage-dependent ion channels in Saccharomyces cerevisiae.’, Philosophical transactions of the Royal Society of London. Series B, Biological sciences. doi: 10.1098/rstb.1992.0129.

Bertl A and Slayman CL (1990) ‘Cation-selective channels in the vacuolar membrane of Saccharomyces: Dependence on calcium, redox state, and voltage’, Proceedings of the National Academy of Sciences of the United States of America, 87(20), pp. 7824–7828. doi: 10.1073/pnas.87.20.7824. [PubMed: 1700419]

Cao E et al. (2013) ‘TRPV1 structures in distinct conformations reveal activation mechanisms’, Nature. doi: 10.1038/nature12823.

Chang Y et al. (2010) ‘Properties of the intracellular transient receptor potential (TRP) channel in yeast, Yvc1’, FEBS Letters. doi: 10.1016/j.febslet.2009.12.035.

Chen VB et al. (2010a) ‘MolProbity: All-atom structure validation for macromolecular crystallography’, Acta Crystallographica Section D: Biological Crystallography, 66(1), pp. 12–21. doi: 10.1107/S0907444909042073. [PubMed: 20057044]

Chen VB et al. (2010b) ‘MolProbity: All-atom structure validation for macromolecular crystallography’, Acta Crystallographica Section D: Biological Crystallography. 2009/12/21, 66(1), pp. 12–21. doi: 10.1107/S0907444909042073. [PubMed: 20057044]

Cruickshank CC et al. (1997) ‘Estimation of the pore size of the large-conductance mechanosensitive ion channel of Escherichia coli’, Biophysical journal, 73(4), pp. 1925–1931. doi: 10.1016/S0006-3495(97)78223-7. [PubMed: 9336188]

Cui J et al. (2009) ‘Calcium homeostasis and signaling in yeast cells and cardiac myocytes’, FEMS Yeast Research, 9(8), pp. 1137–1147. doi: 10.1111/j.1567-1364.2009.00552.x. [PubMed: 19678847]

Diver MM, Cheng Y and Julius D (2019) ‘Structural insights into TRPM8 inhibition and desensitization’, Science. doi: 10.1126/science.aax6672.

Dolinsky TJ et al. (2004) ‘PDB2PQR: An automated pipeline for the setup of Poisson-Boltzmann electrostatics calculations’, Nucleic Acids Research, 32(WEB SERVER ISS.), pp. W665–W667. doi: 10.1093/nar/gkh381. [PubMed: 15215472]

Dunn T, Gable K and Beeler T (1994) ‘Regulation of cellular Ca2+ by yeast vacuoles.’, Journal of Biological Chemistry, 269(10), pp. 7273–7278. Available at: http://www.jbc.org/content/269/10/7273.abstract.

Emsley P and Cowtan K (2004) ‘Coot: Model-building tools for molecular graphics’, Acta Crystallographica Section D: Biological Crystallography, 60(12 I), pp. 2126–2132. doi: 10.1107/S0907444904019158. [PubMed: 15572765]

Fiser A, Do RK and Sali A (2000) ‘Modeling of loops in protein structures.’, Protein science : a publication of the Protein Society, 9(9), pp. 1753–1773. doi: 10.1110/ps.9.9.1753. [PubMed: 11045621]

Gao Y et al. (2016) ‘TRPV1 structures in nanodiscs reveal mechanisms of ligand and lipid action’, Nature, 534(7607), pp. 347–351. doi: 10.1038/nature17964. [PubMed: 27281200]

Geragotelis AD et al. (2020) ‘Voltage-dependent structural models of the human Hv1 proton channel from long-timescale molecular dynamics simulations’, Proceedings of the National Academy of Sciences of the United States of America. doi: 10.1073/pnas.1920943117.

Glykos NM (2006) ‘Carma: A Molecular Dynamics Analysis Program’, Journal of computational chemistry, 27(14), pp. 1765–1768. doi: 10.1002/jcc. [PubMed: 16917862]

Gumbart J et al. (2012) ‘Constant electric field simulations of the membrane potential illustrated with simple systems’, Biochimica et Biophysica Acta (BBA) - Biomembranes, 1818(2), pp. 294–302. doi: 10.1016/j.bbamem.2011.09.030. [PubMed: 22001851]

Halachmi D and Eilam Y (1989) ‘Cytosolic and vacuolar Ca2+ concentrations in yeast cells measured with the Ca2+-sensitive fluorescence dye indo-1’, FEBS Letters, 256(1-2), pp. 55–61. doi: 10.1016/0014-5793(89)81717-X. [PubMed: 2680600]

Hamamoto S et al. (2018) ‘In vitro and in vivo characterization of modulation of the vacuolar cation channel TRPY1 from Saccharomyces cerevisiae’, FEBS Journal, 285(6), pp. 1146–1161. doi: 10.1111/febs.14399.

Hellmich UA and Gaudet R (2014) ‘Structural Biology of TRP Channels BT - Mammalian Transient Receptor Potential (TRP) Cation Channels: Volume II’, in Nilius B and Flockerzi V (eds). Cham: Springer International Publishing, pp. 963–990. doi: 10.1007/978-3-319-05161-1_10.

Hille B (2001) Ion Channels of Excitable Membranes. 3rd edn. Sinauer Associates is an imprint of Oxford University Press.

Hodges RS et al. (1988) ‘Antigen-antibody interaction. Synthetic peptides define linear antigenic determinants recognized by monoclonal antibodies directed to the cytoplasmic carboxyl terminus of rhodopsin.’, The Journal of biological chemistry, 263(24), pp. 11768–11775. [PubMed: 2457026]

Hohmann S (2002) ‘Osmotic Stress Signaling and Osmoadaptation in Yeasts’, Microbiology and Molecular Biology Reviews, 66(2), pp. 300–372. doi: 10.1128/mmbr.66.2.300-372.2002. [PubMed: 12040128]

Hohmann S, Krantz M and Nordlander B (2007) ‘Yeast Osmoregulation’, in Häussinger D and Sies HBT-M in E. (eds) Methods in Enzymology. Academic Press, pp. 29–45. doi: 10.1016/S0076-6879(07)28002-4.

Huffer KE et al. (2020) ‘Global alignment and assessment of TRP channel transmembrane domain structures to explore functional mechanisms’, bioRxiv, p. 2020.05.14.096792. doi: 10.1101/2020.05.14.096792.

Hughes TET et al. (2018) ‘Structural basis of TRPV5 channel inhibition by econazole revealed by cryo-EM’, Nature Structural and Molecular Biology. doi: 10.1038/s41594-017-0009-1.

Humphrey W, Dalke A and Schulten K (1996) ‘VMD: Visual molecular dynamics’, Journal of Molecular Graphics. doi: 10.1016/0263-7855(96)00018-5.

Jensen MØ et al. (2012) ‘Mechanism of voltage gating in potassium channels.’, Science (New York, N.Y.), 336(6078), pp. 229–233. doi: 10.1126/science.1216533.

Jin P et al. (2017) ‘Electron cryo-microscopy structure of the mechanotransduction channel NOMPC’, Nature, 547(7661), pp. 118–122. doi: 10.1038/nature22981. [PubMed: 28658211]

Jorgensen WL et al. (1983) ‘Comparison of simple potential functions for simulating liquid water’, The Journal of Chemical Physics. doi: 10.1063/1.445869.

Julius D (2013) ‘TRP Channels and Pain’, Annual Review of Cell and Developmental Biology, 29(1), pp. 355–384. doi: 10.1146/annurev-cellbio-101011-155833.

Kelley LA et al. (2015) ‘The Phyre2 web portal for protein modeling, prediction and analysis’, Nature Protocols. doi: 10.1038/nprot.2015.053.

Lippert RA et al. (2013) ‘Accurate and efficient integration for molecular dynamics simulations at constant temperature and pressure’, Journal of Chemical Physics. doi: 10.1063/1.4825247.

Moiseenkova-Bell VY et al. (2008) ‘Structure of TRPV1 channel revealed by electron cryomicroscopy’, Proceedings of the National Academy of Sciences of the United States of America. doi: 10.1073/pnas.0711835105.

Moldovan R, Chapman-McQuiston E and Wu XL (2007) ‘On Kinetics of Phage Adsorption’, Biophysical Journal, 93(1), pp. 303–315. doi: 10.1529/biophysj.106.102962. [PubMed: 17434950]

Moriarty NW, Grosse-Kunstleve RW and Adams PD (2009a) ‘Electronic ligand builder and optimization workbench (eLBOW): A tool for ligand coordinate and restraint generation’, Acta Crystallographica Section D: Biological Crystallography, 65(10), pp. 1074–1080. doi: 10.1107/S0907444909029436. [PubMed: 19770504]

Moriarty NW, Grosse-Kunstleve RW and Adams PD (2009b) ‘Electronic ligand builder and optimization workbench (eLBOW): A tool for ligand coordinate and restraint generation’, Acta

Crystallographica Section D: Biological Crystallography, 65(10), pp. 1074–1080. doi: 10.1107/S0907444909029436. [PubMed: 19770504]

Nascimbeni AC, Codogno P and Morel E (2017) 'Phosphatidylinositol-3-phosphate in the regulation of autophagy membrane dynamics', FEBS Journal. doi: 10.1111/febs.13987.

Nikolaev YA et al. (2019) 'Mammalian TRP ion channels are insensitive to membrane stretch', Journal of Cell Science. doi: 10.1242/jcs.238360.

Paknejad N and Hite RK (2018) 'Structural basis for the regulation of inositol trisphosphate receptors by Ca2+ and IP3', Nature Structural and Molecular Biology. 2018/7/16, 25(8), pp. 660–668. doi: 10.1038/s41594-018-0089-6.

Palmer CP et al. (2001) 'A TRP homolog in Saccharomyces cerevisiae forms an intracellular Ca2+-permeable channel in the yeast vacuolar membrane', Proceedings of the National Academy of Sciences of the United States of America. doi: 10.1073/pnas.141036198.

Pettersen EF et al. (2004) 'UCSF Chimera--a visualization system for exploratory research and analysis.', J Comput Chem, 25, pp. 1605–1612. doi: doi:10.1002/jcc.20084. [PubMed: 15264254]

Phillips JC et al. (2005) 'Scalable molecular dynamics with NAMD.', Journal of computational chemistry, 26(16), pp. 1781–1802. doi: 10.1002/jcc.20289. [PubMed: 16222654]

Phillips JC et al. (2020) 'Scalable molecular dynamics on CPU and GPU architectures with NAMD', Journal of Chemical Physics. doi: 10.1063/5.0014475.

Pumroy RA et al. (2020) 'Structural insights into the gating mechanisms of TRPV channels', Cell Calcium, 87. doi: 10.1016/j.ceca.2020.102168.

Ramsey IS et al. (2006) 'A voltage-gated proton-selective channel lacking the pore domain', Nature. doi: 10.1038/nature04700.

Ramsey IS, Delling M and Clapham DE (2006) 'AN INTRODUCTION TO TRP CHANNELS', Annual Review of Physiology, 68(1), pp. 619–647. doi: 10.1146/annurev.physiol.68.040204.100431.

Rohou A and Grigorieff N (2015) 'CTFFIND4: Fast and accurate defocus estimation from electron micrographs', Journal of Structural Biology, 192(2), pp. 216–221. doi: 10.1016/j.jsb.2015.08.008. [PubMed: 26278980]

Rosasco MG, G. S. (2017) 'TRP Channels: What Do They Look Like?', in Neurobiology of TRP Channels. 2nd edition. CRC Press/Taylor & Francis. doi: 10.4324/9781315152837-1.

Roy A, Kucukural A and Zhang Y (2010) 'I-TASSER: A unified platform for automated protein structure and function prediction', Nature Protocols. 2010/3/25, 5(4), pp. 725–738. doi: 10.1038/nprot.2010.5. [PubMed: 20360767]

Sakipov S, Sobolevsky AI and Kurnikova MG (2018) 'Ion Permeation Mechanism in Epithelial Calcium Channel TRVP6', Scientific Reports, 8(1), pp. 1–13. doi: 10.1038/s41598-018-23972-5. [PubMed: 29311619]

Scheres SHW (2012) 'RELION: Implementation of a Bayesian approach to cryo-EM structure determination', Journal of Structural Biology, 180(3), pp. 519–530. doi: 10.1016/j.jsb.2012.09.006. [PubMed: 23000701]

Scheres SHW (2016) 'Processing of Structurally Heterogeneous Cryo-EM Data in RELION', in Crowther RABT-M in E. (ed.) Methods in Enzymology. Academic Press, pp. 125–157. doi: 10.1016/bs.mie.2016.04.012.

Schrodinger L (2015) 'The PyMOL Molecular Graphics System, Version 1.8'.

Sethi A et al. (2009) 'Dynamical networks in tRNA: Protein complexes', Proceedings of the National Academy of Sciences of the United States of America. doi: 10.1073/pnas.0810961106.

Shaw DE et al. (2008) 'Anton, a special-purpose machine for molecular dynamics simulation', Communications of the ACM. doi: 10.1145/1364782.1364802.

Smart OS et al. (1996) 'HOLE: A program for the analysis of the pore dimensions of ion channel structural models', Journal of Molecular Graphics. doi: 10.1016/S0263-7855(97)00009-X.

Sotomayor M et al. (2007) 'Ion conduction through MscS as determined by electrophysiology and simulation.', Biophysical journal, 92(3), pp. 886–902. doi: 10.1529/biophysj.106.095232. [PubMed: 17114233]

Su Z et al. (2007) ‘Yeast gain-of-function mutations reveal structure-function relationships conserved among different subfamilies of transient receptor potential channels’, Proceedings of the National Academy of Sciences of the United States of America. doi: 10.1073/pnas.0708584104.

Su Z et al. (2009) ‘Mechanical force and cytoplasmic Ca2+ activate yeast TRPY1 in parallel’, Journal of Membrane Biology, 227(3), pp. 141–150. doi: 10.1007/s00232-009-9153-9. [PubMed: 19219385]

Su Z et al. (2011) ‘The core domain as the force sensor of the yeast mechanosensitive TRP channel’, Journal of General Physiology, 138(6), pp. 627–640. doi: 10.1085/jgp.201110693.

Tang Q et al. (2018) ‘Structure of the receptor-activated human TRPC6 and TRPC3 ion channels’, Cell Research. doi: 10.1038/s41422-018-0038-2.

Teng J et al. (2015) ‘The force-from-lipid (FFL) principle of mechanosensitivity, at large and in elements’, Pflugers Archiv : European journal of physiology. 2014/6/03, 467(1), pp. 27–37. doi: 10.1007/s00424-014-1530-2. [PubMed: 24888690]

Tsuji T and Fujimoto T (2018) ‘Lipids and lipid domains of the yeast vacuole’, Biochemical Society Transactions, 46(5), pp. 1047–1054. doi: 10.1042/BST20180120. [PubMed: 30242116]

Vanommeslaeghe K and Mackerell AD (2015) ‘CHARMM additive and polarizable force fields for biophysics and computer-aided drug design’, Biochimica et Biophysica Acta - General Subjects. doi: 10.1016/j.bbagen.2014.08.004.

Wang Q et al. (2020) ‘Lipid Interactions of a Ciliary Membrane TRP Channel: Simulation and Structural Studies of Polycystin-2’, Structure, 28(2), pp. 169–184.e5. doi: 10.1016/j.str.2019.11.005. [PubMed: 31806353]

Winkler PA et al. (2017) ‘Electron cryo-microscopy structure of a human TRPM4 channel’, Nature. doi: 10.1038/nature24674.

Yan Z et al. (2013) ‘Drosophila NOMPC is a mechanotransduction channel subunit for gentle-touch sensation’, Nature. 2012/12/09, 493(7431), pp. 221–225. doi: 10.1038/nature11685. [PubMed: 23222543]

Yang J and Zhang Y (2015) ‘I-TASSER server: New development for protein structure and function predictions’, Nucleic Acids Research. 2015/4/16, 43(W1), pp. W174–W181. doi: 10.1093/nar/gkv342. [PubMed: 25883148]

Zhang W et al. (2015) ‘Ankyrin Repeats Convey Force to Gate the NOMPC Mechanotransduction Channel’, Cell. doi: 10.1016/j.cell.2015.08.024.

Zhao J et al. (2020) ‘Irritant-evoked activation and calcium modulation of the TRPA1 receptor’, Nature. doi: 10.1038/s41586-020-2480-9.

Zhao J and Blunck R (2016) ‘The isolated voltage sensing domain of the Shaker potassium channel forms a voltage-gated cation channel’, eLife. doi: 10.7554/eLife.18130.

Zheng SQ et al. (2017a) ‘MotionCor2: Anisotropic correction of beam-induced motion for improved cryo-electron microscopy’, Nature Methods, 14(4), pp. 331–332. doi: 10.1038/nmeth.4193. [PubMed: 28250466]

Zheng SQ et al. (2017b) ‘MotionCor2: Anisotropic correction of beam-induced motion for improved cryo-electron microscopy’, Nature Methods. 2017/2/27, 14(4), pp. 331–332. doi: 10.1038/nmeth.4193. [PubMed: 28250466]

Zhou X et al. (2007) ‘Yeast screens show aromatic residues at the end of the sixth helix anchor transient receptor potential channel gate’, Proceedings of the National Academy of Sciences of the United States of America. doi: 10.1073/pnas.0704039104.

Zhou XL et al. (2003) ‘The transient receptor potential channel on the yeast vacuole is mechanosensitive’, Proceedings of the National Academy of Sciences of the United States of America, 100(12), pp. 7105–7110. doi: 10.1073/pnas.1230540100. [PubMed: 12771382]

Zivanov J et al. (2018) ‘New tools for automated high-resolution cryo-EM structure determination in RELION-3’, eLife. Edited by Egelman EH and Kuriyan J, 7, p. e42166. doi: 10.7554/eLife.42166. [PubMed: 30412051]

Zubcevic L and Lee S-Y (2019) ‘The role of π-helices in TRP channel gating’, Current Opinion in Structural Biology, 58, pp. 314–323. doi: 10.1016/j.sbi.2019.06.011. [PubMed: 31378426]

Highlights

- Cryo-EM reveals a closed pore structure of tetrameric TRPY1.
- TRPY1 displays conserved TM domain but distinct folds in NTD and CTD.
- Two occupied Ca^{2+}-binding sites per subunit, one activating and the other inhibiting.
- One inhibitory PI(3)P lipid per subunit gets co-purified with the channel.

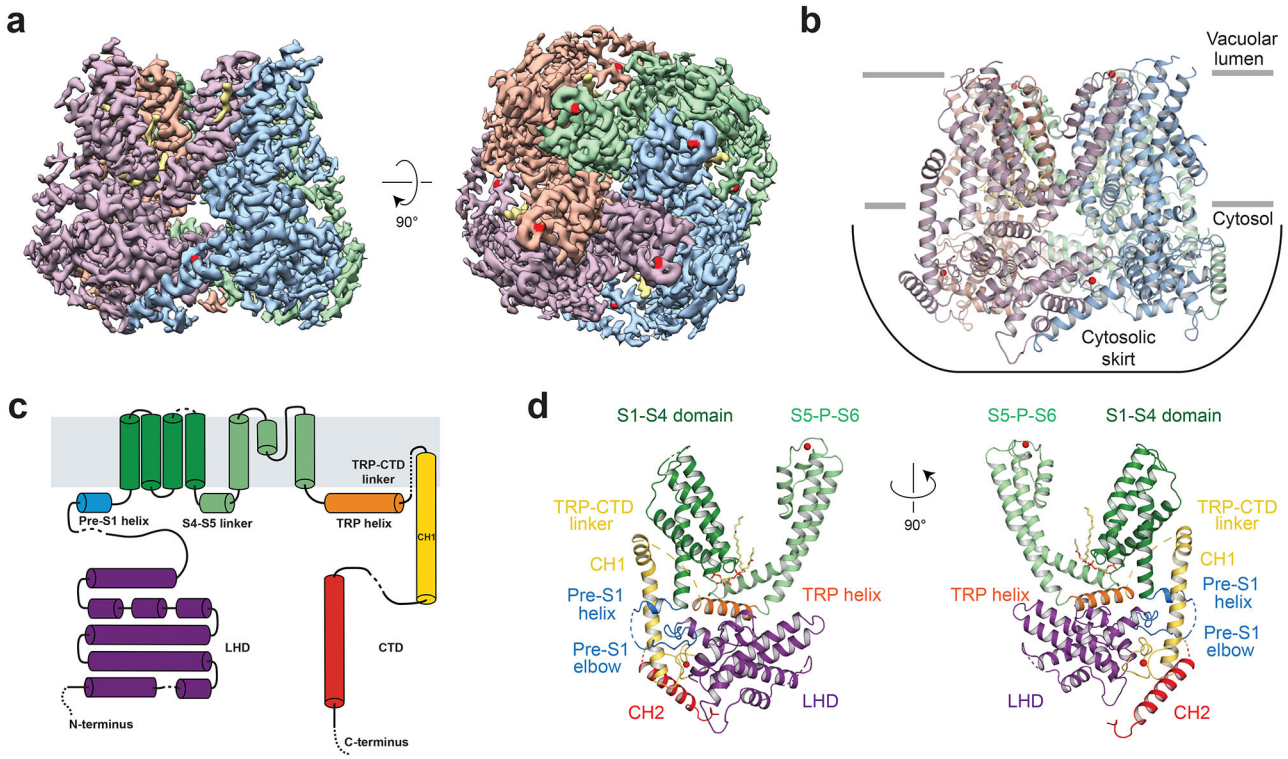

Figure 1. Overall TRPY1 architecture. See also Figures S1-S3.

a, TRPY1 homo-tetramer density at 3.1 Å resolution, shown at threshold level 0.031 in Chimera(Pettersen, 2004). Side view parallel to the membrane (left) and view from the vacuolar lumen side (right) are displayed to show domain-swapped architecture and positions of lipids (khaki) and Ca^{2+} (red). **b**, Cartoon representation of the atomic model built in the cryo-EM density. Due to ambiguity, models for the lipid (khaki) at the top right corner in (a, left) were not built. Due to the absence of ankyrin-repeats, a cytosolic skirt is formed by the distinctive arrangement of the different cytosolic domains, loops, and parts of helices, as labelled. Cartoon colors are matched to the electron density in **(a). c,** Schematic domain organization of a TRPY1 subunit. Dashed lines indicate unmodeled traces in the flexible regions containing weak density. Helices and loops are not drawn to scale. LHD = Linker helical domain, LH = Linker helix, CTD = C-terminal domain, CH1 = C-terminal helix 1, CH2 = C-terminal helix 2. **d,** Cartoon representation of the domain organization in a TRPY1 subunit to show relative positions of different domains, using matching colors from **(c)**.

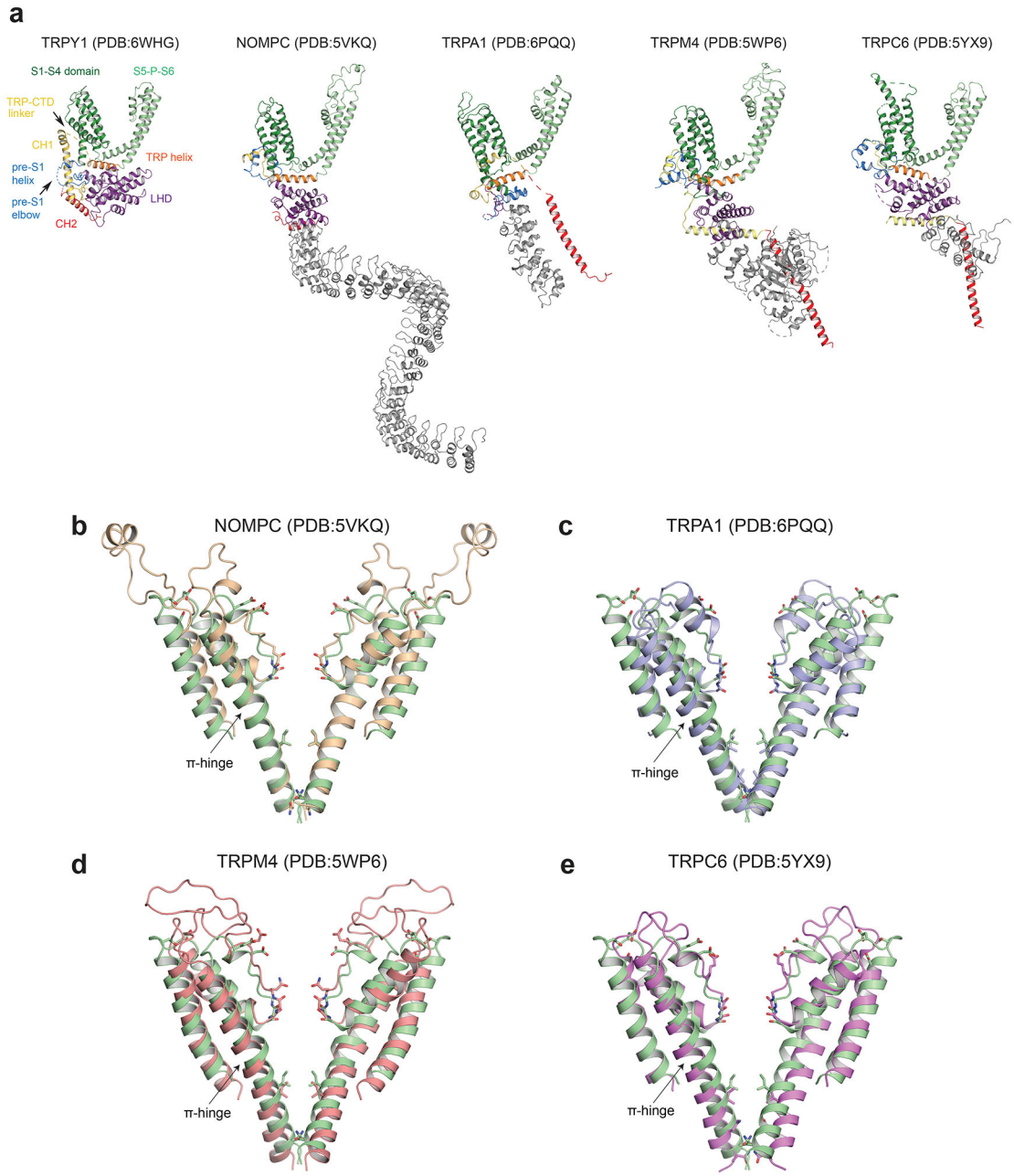

Figure 2. Comparison of TRPY1's overall architecture and ion permeation pathway with other TRP channels, Related to Figure 4.

a, A subunit from the TRPY1 structure derived from the current study (extreme left) with domains colored differently and labelled. Subunits from the TRP channels possessing structural similarity with TRPY1 are displayed with their domains color-matched with TRPY1. The extra domains which are absent from the TRPY1 structure are colored in grey. **b, c, d and e,** Drosophila NOMPC (**b**) and TRPA1 (**c**), TRPM4 (**d**) and TRPC6 (**e**) from human are pore-aligned on S5 and S6 helices to TRPY1 to show similarity. Models are colored as: TRPY1: pale green, NOMPC: wheat, TRPA1: light blue, TRPM4: salmon and TRPC6: violet.

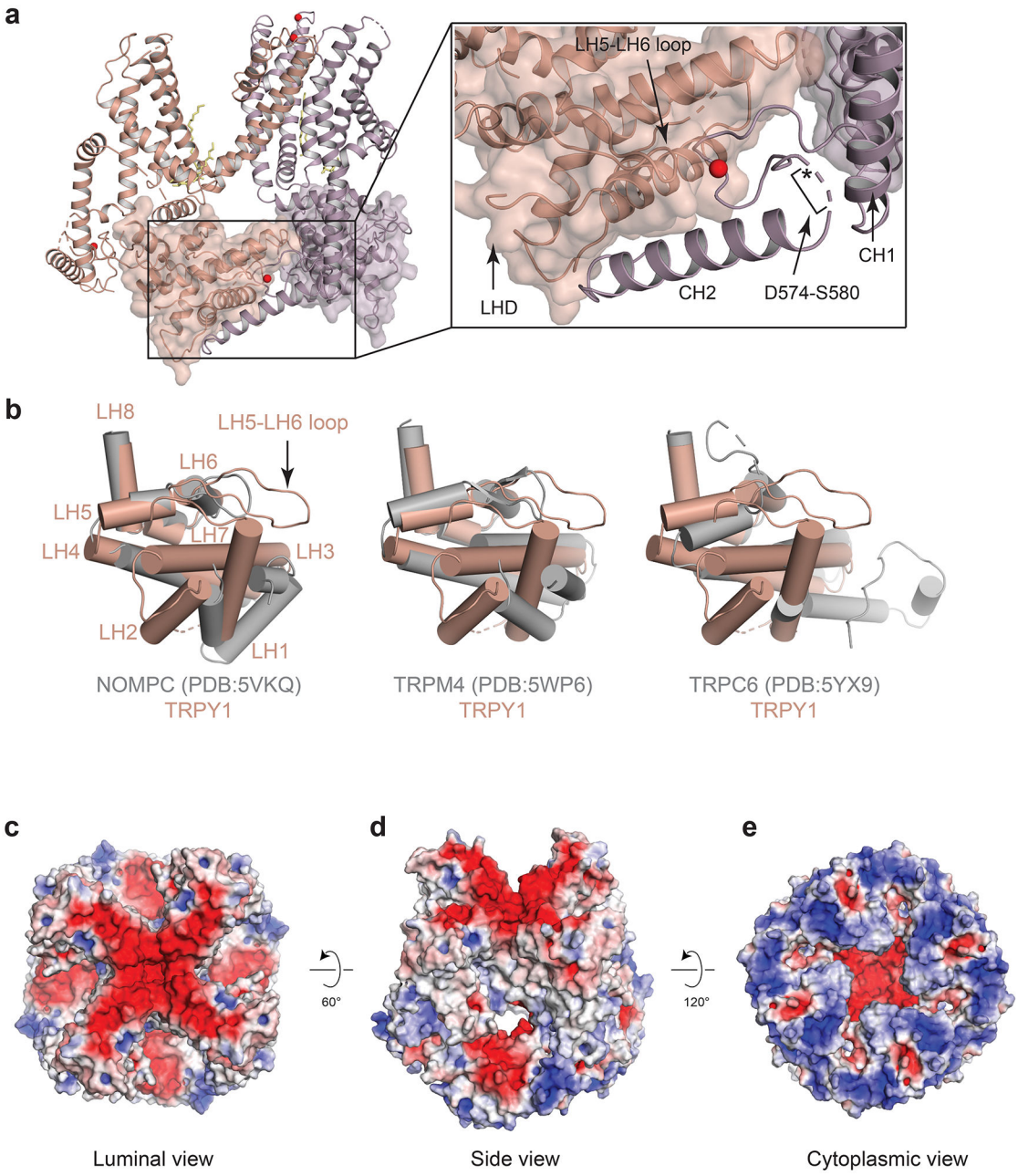

Figure 3. Distinct structural features of TRPY1 LHD and electrostatic potential surface of TRPY1, Related to Figure 4.

(a) Two subunits (salmon and plum cartoons) of TRPY1 shown to display close interaction of LHD and CTD from neighboring subunits. Both LHDs are also represented as transparent surface generated from the model. The cytosolic and vacuolar lumen Ca^{2+} ions are in red. The position of C-terminal acidic patch is marked by an asterisk. Due to possible flexibility, density between D574-S580 is absent and not modeled. **(b)** TRPY1 LHD structure in comparison to LHDs from NOMPC, TRPM4 and TRPC6. **c, d and e,** Luminal **(c)**, tilted side **(d)** and cytosolic **(e)** views are shown for the electrostatic potential surface generated from TRPY1 2mM Ca^{2+} condition model. Negative and positive electrostatic potentials are

colored as red and blue, respectively. Ca^{2+} ions and PI(3)P lipids were excluded before calculating the surface.

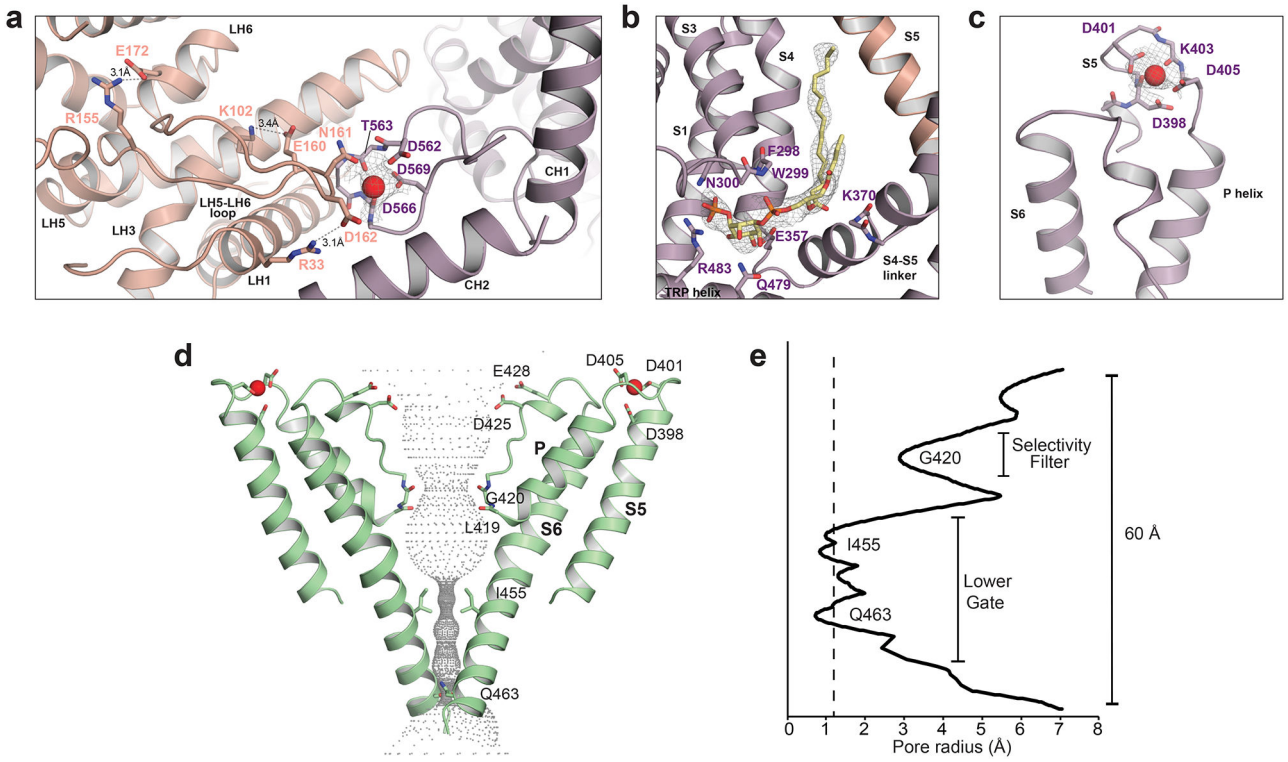

Figure 4. Ca^{2+} and PI(3)P binding sites, and ion permeation pathway. See also Figures 2, 3, S4.

a, Cytosolic Ca^{2+}-binding site. Ca^{2+} is displayed in red. Interacting protein residues are displayed in sticks and labelled accordingly. **b,** PI(3)P binding site. The atomic model of PI(3)P lipid is displayed in sticks with elements colored as: carbon in khaki, phosphorous in orange and oxygen in red. **c,** Ca^{2+}-binding sites at the vacuolar lumen side. Shown as in (a). Densities for the cytosolic Ca^{2+}, PI(3)P and luminal Ca^{2+} are isolated from the original map and displayed in grey meshes at sigma level 1.5 in (a), (b) and (c), respectively. **d,** Cartoon representation of TRPY1 ion permeation pathway. Ca^{2+} is displayed in red. Grey dots illustrate pore size as determined by HOLE. **e,** Graphical representation of the radius of the TRPY1 pore as a function of the distance along the ion permeation pathway. The dashed line indicates the radius of a dehydrated Ca^{2+}.

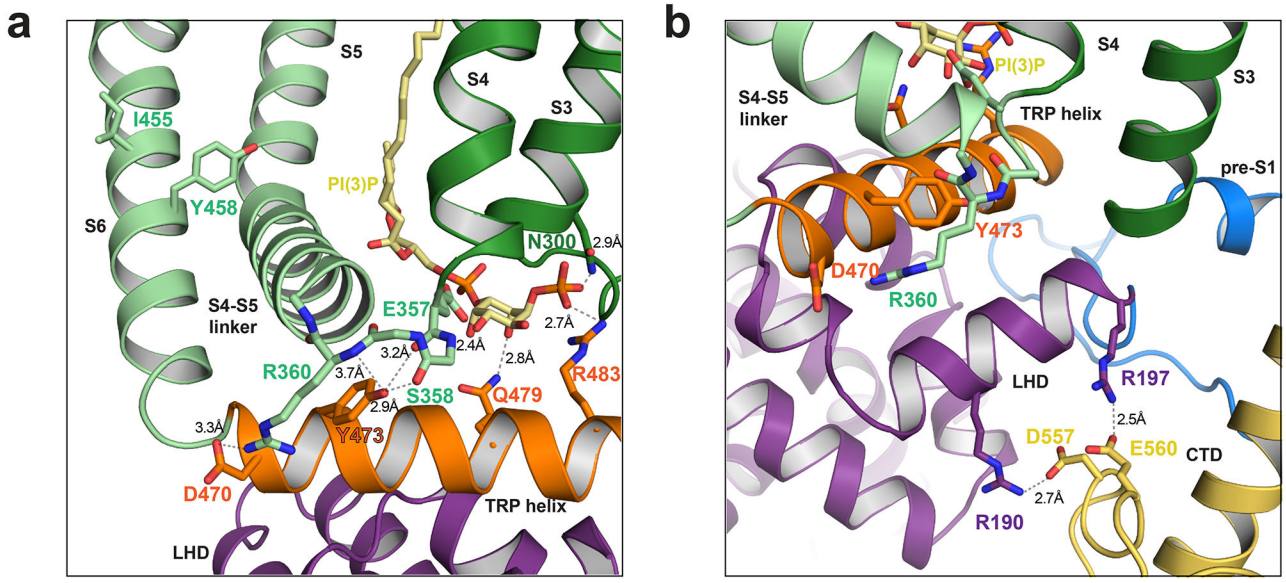

Figure 5. Interaction network in the closed state of TRPY1.

a, Interaction network between S4-S5 linker (green), TRP helix (orange) and PI(3)P (khaki) to stabilize the closed state of TRPY1. **b,** Interactions between LHD and CTD.

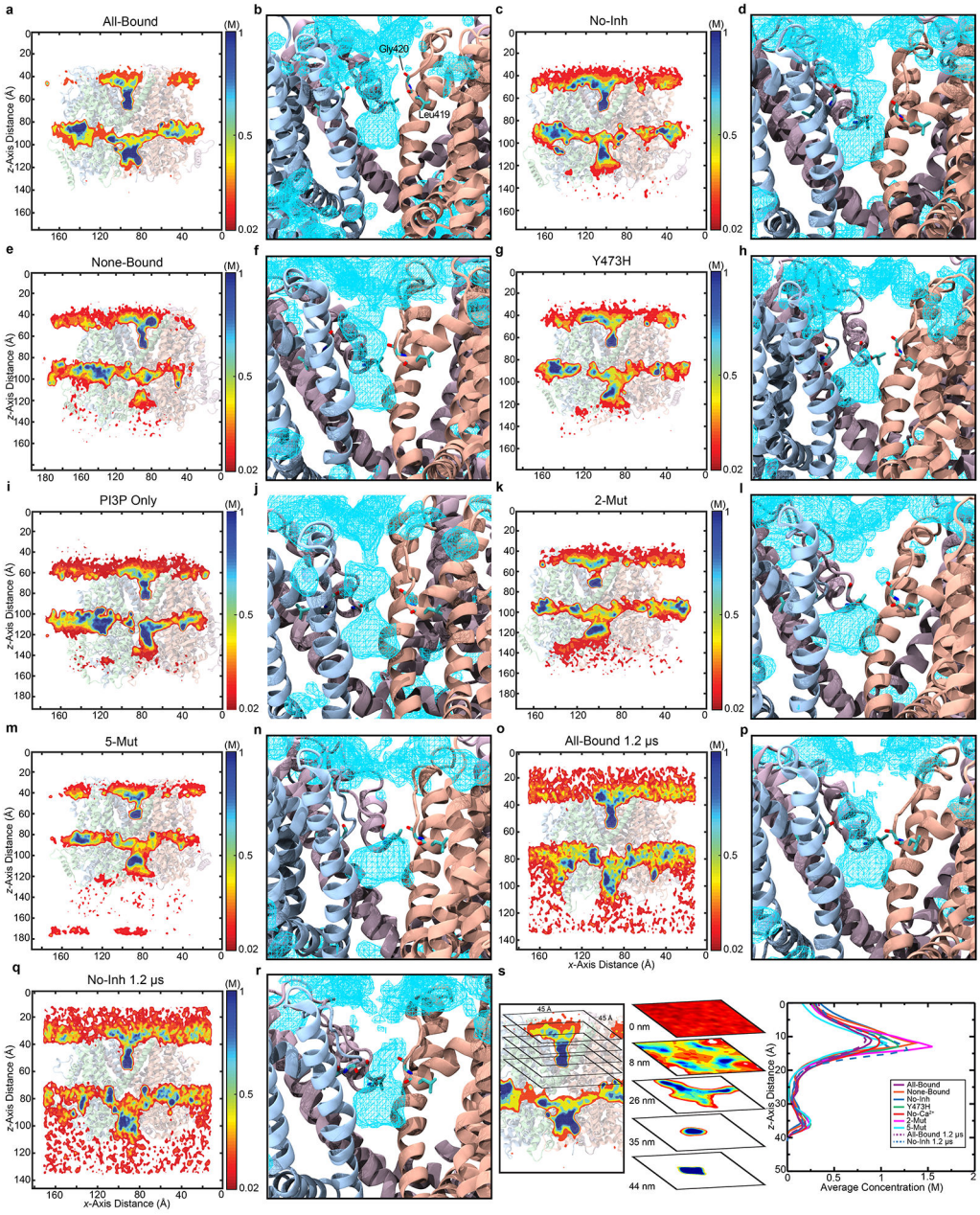

Figure 6. Ion density of vertical configuration simulations show that removal of inhibitory Ca^{2+} and introduction of mutations increases ion access to the pore. See also Table S1 and Figure 7.

The density of K+ ions is shown at the origin of the simulation system, corresponding to the center of the pore, for each system in the *x-z* plane (**a, c, e, g, i, k, m, o, q**). The density of K+ ions represented as a magenta mesh (**b, d, f, h, j, l, n, p, r**). The All-Bound system (**a**) exhibits reduced density in the luminal side of the membrane due to bound Ca^{2+} compared to all systems in which the luminal Ca^{2+} is removed. In addition, systems with mutations (**g, k, m**) exhibit increased density beyond the selectivity filter. **s,** Ion density is quantified for each system by taking the average density on successive squares in the *x-y* plane along the *z*-axis.

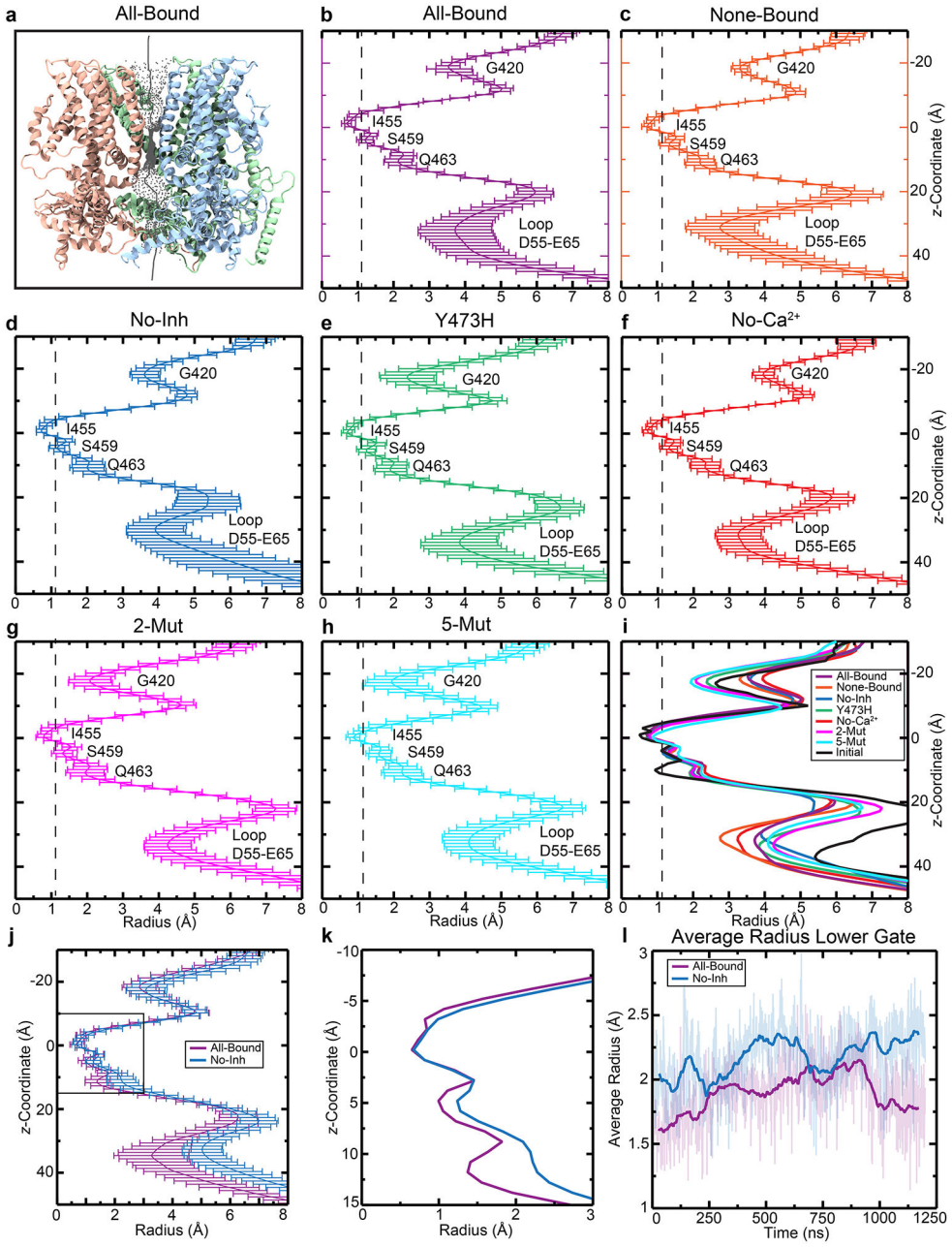

Figure 7. Simulations predict pore widening upon removal of PI(3)P and cytosolic skirt stabilization by Ca^{2+}. See also Table S1 and Figure 6.

a, Pore size through the entire channel illustrated by grey dots, and the optimal path shown by a grey line. For ease of viewing, chain A has been omitted. Protein structure and optimal conduction path are taken from a single frame of Sim1. **b-h,** Pore radius averaged over the entire 100 ns trajectories for each system, with standard deviations for each value shown at the associated location in the *z*-axis. Important residues or motifs are indicated, and a dashed line marks the size of a dehydrated Ca^{2+} ion. **i,** The average pore radius overlaid for each system, with the initial structure (black; before simulation) that contains all modeled loops. **j**, The No-Inh system exhibits a larger radius averaged over a microsecond-long simulation

than what is observed for the All-Bound system, both at the lower gate (0 to 15 Å) and at the cytosolic skirt (20 to 40 Å). **k,** A closer view of the pore radius profile focused on the lower-gate regions, box in (**j**). **l**, The average radius at the lower gate (−10 to 15 Å) was larger in the No-Inh system throughout the trajectory.

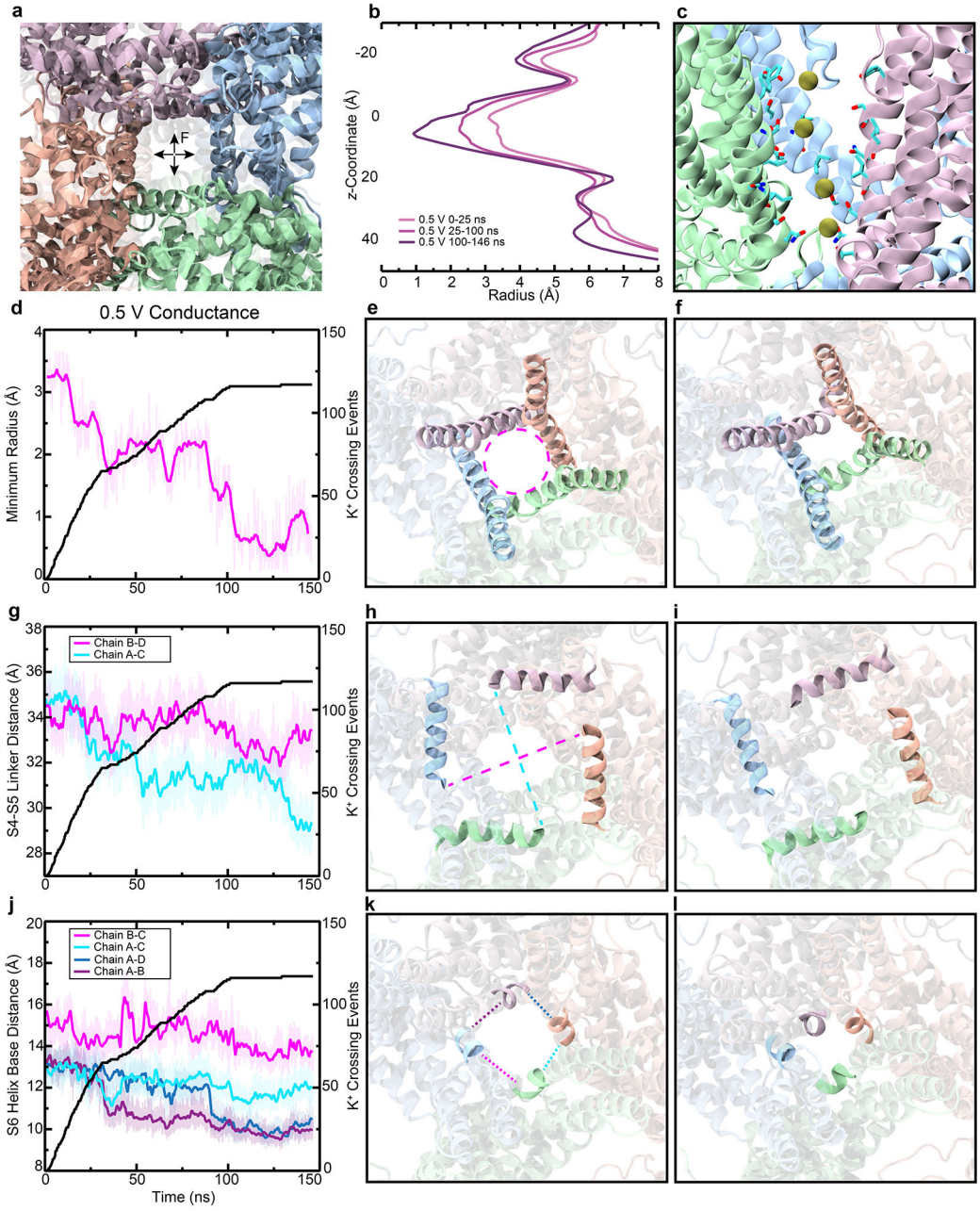

Figure 8. Simulating membrane voltage with an open state model of TRPY1 reveals the structural elements important for ion conduction. See also Table S1, Supplementary Movies 1, 2.

a, The open state (opaque) overlaid with the closed state (transparent), before force is applied. **b**, The average radius profile along the pore is shown for the 150 ns voltage simulation between 0-25 ns (light pink), 25-100 ns (medium pink), and 100-146 ns (dark pink). **c,** Residues that participate in shuttling the K^+ ions through the pore are shown for chains A, B, and C (chain D omitted for clarity). K+ ions are shown in gold spheres. **d,** The minimum radius (pink) is overlaid with the K+ permeation events (black) during the voltage simulation. Large decreases in the minimum radius correlate with decreases in conductance

at ~ 25 ns and ~ 85 ns. The S6 helices are shown before (**e**) and after (**f**) the simulation. **g,** The distance between the Cα carbons of residue 376 of the indicated chains are shown overlaid with the K^+ permeation events. The measured distances from (**g**) are shown before (**h**) and after (**i**) the simulation. **j**, The distances between the center of mass of residues 458-462, corresponding to the base of the S6 helix, is overlaid with K+ permeation events. The measured distances from (**j**) are shown before (**k**) and after (**l**) the simulation.

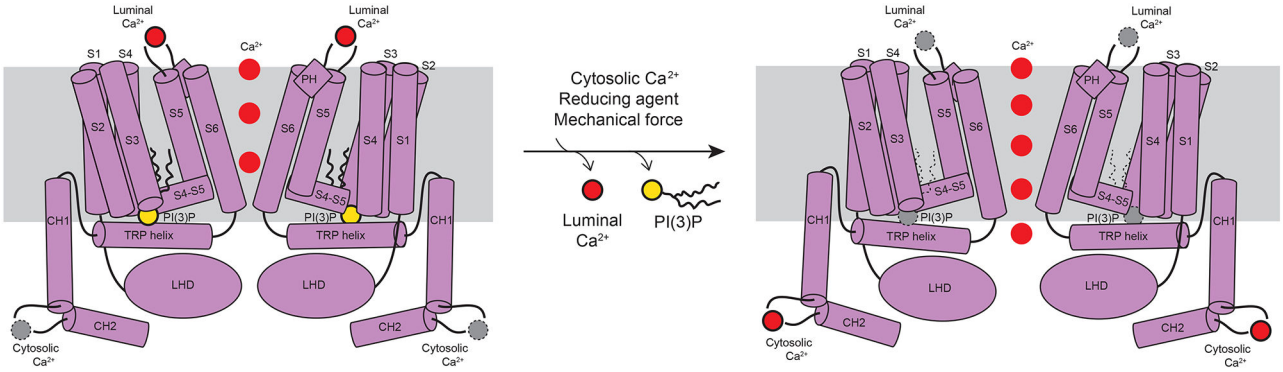

Figure 9. Proposed gating mechanism of TRPY1.

Schematic diagram illustrating potential gating mechanism for TRPY1. On each side, two diagonal subunits of TRPY1 are shown in purple. PI(3)P is shown in khaki, and the red circles indicate the TRPY1 Ca^{2+}-binding sites and the flow of Ca^{2+}. For simplicity, the diagonal subunits are shown in the same topology.

Table 1.

Refinement statistics for Ca^{2+}-bound TRPY1 map (EMDB: 21672) and model (PDB: 6WHG).

Data collection and processing	TRPY1, 2mM Ca^{2+} condition
Magnification	81,000x
Detector mode	super-resolution
Voltage (kV)	300
Defocus range (μm)	0.5-2.5
Pixel size (Å)	1.06
Total extracted particles (no.)	3,120,706
Refined particles (no.)	254,509
Final particles (no.)	55,593
Symmetry imposed	C4
Map sharpening *B* factor ($Å^2$)	−94.37
Map resolution (Å)	3.1
FSC threshold	0.143
Model Refinement	
Model resolution cut-off (Å)	3.1
Model composition	
Nonhydrogen atoms	17116
Protein residues	2092
Ligands	PWE: 4, CA: 8
R.M.S. deviations	
Bond Lengths (Å)	0.009
Bond angles (°)	1.129
Validation	
Molprobity score	1.47
Clashscore	2.65
Poor rotamers (%)	1.98
CαBLAM outliers (%)	1.60
EMRinger score	3.24
Ramachandran plot	
Favored (%)	96.87
Allowed (%)	3.13
Disallowed (%)	0.00

KEY RESOURCES TABLE

REAGENT or RESOURCE	SOURCE	IDENTIFIER
Antibodies		
1D4 primary antibody	(Hodges et al., 1988)	N/A
Chemicals, peptides, and recombinant proteins		
$CaCl_2$	Fisher Chemical	Cat# C70-500
Tris-Base	Fisher BioReagents	Cat# BP152-1
Sucrose	Fisher Chemical	Cat# S3-212
EDTA	Fisher BioReagents	Cat# BP120-1
Protease inhibitor cocktail	Sigma	Cat# P8215
PMSF	Acros Organics	Cat# 215740500
HEPES	Sigma	Cat# H3375-500G
NaCl	Fisher BioReagents	Cat# BP358-10
Glycerol	Fisher BioReagents	Cat# BP229-4
Digitonin	Millipore	Cat# 300410-5GM
TCEP	Pierce	Cat# PG82090
CnBr-activated sepharose beads	Cytiva	Cat# 17043001
Deposited data		
PDB	This paper, https://www.rcsb.org/	6WHG
EMDB	This paper, https://www.ebi.ac.uk/pdbe/emdb/	EMD-21672
Experimental models: Organisms/strains		
Saccharomyces cerevisiae BJ5457	ATCC	208282
Recombinant DNA		
YepM plasmid vector	(Moiseenkova-Bell et al., 2008)	N/A
Software and algorithms		
RELION	(Scheres, 2012, 2016; Zivanov et al., 2018)	https://www3.mrc-lmb.cam.ac.uk/relion/index.php?title=Main_Page
Coot	(Emsley and Cowtan, 2004)	https://www2.mrc-lmb.cam.ac.uk/personal/pemsley/coot/
Phenix	(Adams et al., 2002)	https://phenix-online.org/documentation/index.html
MotionCor2	(Zheng et al., 2017a; Zivanov et al., 2018)	https://emcore.ucsf.edu/ucsf-software
CTFFIND-4.1	(Rohou and Grigorieff, 2015)	https://grigoriefflab.umassmed.edu/ctffind4
ITASSER	(Roy, Kucukural and Zhang, 2010; Yang and Zhang, 2015)	https://zhanglab.dcmb.med.umich.edu/I-TASSER/
eLBOW	(Moriarty, Grosse-Kunstleve and Adams, 2009a)	https://phenix-online.org/documentation/reference/elbow_gui.html
Molprobity	(Chen et al., 2010a)	http://molprobity.biochem.duke.edu/
EMRinger	(Barad et al., 2015)	https://github.com/fraser-lab/EMRinger
EMAN2.1	(Bell et al., 2016)	https://blake.bcm.edu/emanwiki/EMAN2
HOLE	(Smart et al., 1996)	http://www.holeprogram.org/

REAGENT or RESOURCE	SOURCE	IDENTIFIER
PyMOL	(Schrodinger, 2015)	https://pymol.org/2/
APBS-PDB2PQR	(Dolinsky et al., 2004)	https://server.poissonboltzmann.org/
Chimera	(Pettersen, 2004)	https://www.cgl.ucsf.edu/chimera/
MODELLER	(Fiser, Do and Sali, 2000)	https://salilab.org/modeller/
NAMD 2.12	(Phillips et al., 2005)	http://www.ks.uiuc.edu/Research/namd/
CHARMM36/ TIP3P	(Jorgensen et al., 1983; Vanommeslaeghe and Mackerell, 2015)	http://mackerell.umaryland.edu/charmm_ff.shtml, https://www.charmm.org/
VMD and plugins	(Humphrey, Dalke and Schulten, 1996)	http://mackerell.umaryland.edu/charmm_ff.shtml, https://www.ks.uiuc.edu/Research/vmd/
Carma in VMD	(Glykos, 2006)	http://utopia.duth.gr/~glykos/carma.html
Anton2 simulation	(Shaw et al., 2008)	https://www.deshawresearch.com/